Title
Towards Upcycling Polyethylene Terephthalate (PET) Plastic Waste for Energy Storage

Author
Mirjalili, Arash

Publication Date
2021

UNIVERSITY OF CALIFORNIA
RIVERSIDE

Towards Upcycling Polyethylene Terephthalate (PET) Plastic Waste for Energy Storage

A Dissertation submitted in partial satisfaction
of the requirements for the degree of

Doctor of Philosophy

in

Chemistry

by

Arash Mirjalili

June 2021

Dissertation Committee:
  Professor Mihrimah Ozkan, Co-Chairperson
  Professor Cengiz S. Ozkan, Co-Chairperson
  Professor Ludwig Bartels
  Professor Yadong Yin

The Dissertation of Arash Mirjalili is approved:

Co-Chairperson

Co-Chairperson

University of California, Riverside

Acknowledgments

Herein, I would like to express my most sincere gratitude to all who helped and encouraged me during my Ph.D. study. I am especially grateful for my advisor Prof. Mihrimah Ozkan and co-advisor Prof. Cengiz S. Ozkan for their support, guidance, and encouragement throughout my career. I am thankful to Prof. Ludwig Bartels and Prof. Yadong Yin for serving as my committee members in both the qualifying exam and final defence.

I would like to express my appreciation to all members of the Ozkan lab, with whom I had a lot of wonderful discussions about research topics, science, philosophy, sports, and everyday life. For that, I am thankful to Dr. Bo Dong, Dr. Taner Zerrin, Dr. Fabian Villalobos, Dr. Andrew Patalano, Dr. Daisy Patino, Dr. Jingjing Liu, Pedro Pena, Ruoxu Shang, Yi Ma, Dr. Jeffery Bell, Dr. Rachel Ye, Dr. Changling Li, and Dr. Zafer Mutlu. I am appreciative to our collaborator Dr. Mustafa Kurban for his time and effort for the theoretical calculations presented in this work.

I would like to express my gratitude to Christina Youhas and Barbara Anne Outzen-Hill for their academic assistance throughout my study. I would like to thank Dr. David Kirby Hill whom I was a TA for multiple times. I would also like to take this opportunity to acknowledge and appreciate Dr. Kevin Simpson and Dr. Rena Hayashi for their excellent organization and management skills. They made the TA meetings very efficient and productive. I would also like to thank Prof. Francisco Zaera for making it possible for me

to continue my graduate studies at UCR. I want to thank Prof. Pingyun Feng for her kind help on BET analysis. I would like to thank Dr. Krassimir Bozhilov in CFAMM for TEM measurements.

In addition, I would like to thank my other collaborators outside the group, Prof. Ben Jang and Dr. Xinxiang Cao for their insight and help throughout my graduate studies.

I am also thankful to my parents Fereshteh and Mohammadali, and my brother Siavash for their kindness and support during my graduate studies in the U.S. A very special thanks to my loving fiance Kimia C. Yaghoubi for her unconditional love, encouragement, and support that helped me overcome my obstacles throughout my career.

The text of this work, in part or in full, is a reprint of the material as it appears in the following publication: **Mirjalili, A.**, et al, “Upcycling of Polyethylene Terephthalate Plastic Waste to Microporous Carbon Structure for Energy Storage", **Energy Storage** 2, no. 6 (2020): e201. doi:10.1002/est2.201. The co-authors Dr. Mihri Ozkan, and Dr. Cengiz Ozkan listed in the publication directed and supervised the research which forms the basis for this dissertation. Dr. Mustafa Kurban kindly performed the DFTB+ calculations at the TUBITAK ULAKBIM High Performance and Grid Computing Center (TRUBA resources) in Ankara, Turkey.

Dedicated to my loving family.

ABSTRACT OF THE DISSERTATION

Towards Upcycling Polyethylene Terephthalate (PET) Plastic Waste for Energy Storage

by

Arash Mirjalili

Doctor of Philosophy, Graduate Program in Chemistry
University of California, Riverside, June 2021
Prof. Mihrimah Ozkan, Co-Chairperson
Prof. Cengiz S. Ozkan, Co-Chairperson

Plastic pollution is found everywhere. From lands to oceans and atmosphere, plastic wastes are threatening natural ecosystems and human health. New studies show an alarming increase in the amount of micro and nano-sized plastics found in soil, air, and biomass. With rapid increase in consumption rates of single-use plastics (including masks and gloves due to COVID-19 pandemic) along with a sharp rise of production rates, immediate and sustainable solutions are urgent. To lessen the plastic pollution build-up and keep plastics as a useful and valuable commodity, recycling technologies need to be improved to keep pace with the rising demands. In this work, we investigated the energy storage capability of upcycled Polyethylene Terephthalate (PET) plastic waste. In general, PET has massive utilization in different sectors of industry including textile, packaging, and automotive with nearly a 5% increase in production each year. The pristine upcycled material that was collected via fiberization and controlled carbonization, showed the combination of supercapacitive and pseudocapacitive behaviors. Next, by adding silicon nanoparticles and elemental sulfur, a composite Si-C anode and a S-C cathode were developed, respectively. The generated electrodes were tested in half-cells in a lithium-ion battery setup. We implemented a series of computational, analytical, and electrochemical characterization techniques including DFTB+, Raman, TGA, SEM-EDS, TEM, XRD, BET, CV, GCPL, EIS, and GITT to explore the content of the materials and explain the detected electrochemical performance. The preparation methods are industrially mature and scalable and we hope that this work can bring opportunities for future research and development to tackle plastic pollution and move towards a more sustainable society.

Contents

List of Figures

List of Tables

Chapter 1

Introduction

1.1 Plastic Pollution

Plastics have revolutionized our everyday lives in different ways. They are used for food storage; masks, gloves, and textile production; automotive industry; etc. Since the plastic commercialization in the 1950s, its production has doubled every 11 years.[1] The data shows that by the year 2015, humans have produced about 6.3 billion metric tons (MT) of plastic that is more than 620% increase for the past 45 years.[2] So far, only 9% of the produced plastics were recycled, while 12% were incinerated, and the outstanding 79% have ended up in landfills and oceans. The studies show that by the year 2050, 12 billion MT of plastic waste will be discarded in the natural environment.[2] Plastics are extremely durable, and it takes decades to centuries to be fully decomposed by natural means, making them waste with staying power. In this regard, uncontrolled utilization and disposal of plastics is steering our planet towards a crisis.[3,4] Micro and nano-plastics, which are microscopic plastic particles resulting from physical composition of the plastics, are found in the air that we breathe in, remote areas, and in all major oceans.[5] The world's oceans are hit hard by plastic pollutants and reports are calling for the danger the ecosystems are facing. By the year 2014, more than 5 trillion plastic pieces were afloat at sea.[6] Besides the physical harm the plastics can cause to the wildlife, the chemicals linked to them can hurt living organisms. In addition to their potential toxicity, they can act like chemical absortives once released to the ocean.[7–10] Upon consumption and accumulation of these toxic particles in marine animal tissues and entering the marine food chain, they can be consumed by humans and cause multiple health issues. In this sense, it is recommended to classify plastic waste as hazardous waste once it is discharged into the environment.[10–14] As the equivalent of 65 trash trucks per day of plastic waste is dumped into the oceans in the United States (U.S.) via our land, rivers, and coasts. In July 2018, the U.S. Environmental Protection Agency (USEPA) published the "Advancing Sustainable Materials Management: Facts and Figures Report" that explains the details of the fate of community waste. According to this study, in 2015 a total of 3.14 million tons of community plastic waste were domestically recycled in U.S. This is only about 2.5% (0.88 million tons) of community plastic waste that Americans generated. In 2018, the total amount of plastic waste that was produced in the U.S. saw a 5% growth and reached to about 39.9 million tons. This growth rate is related to the annual development rate of U.S. bottled water sales. In the U.S., almost all bottles of water and other soft drinks are produced from Polyethylene Terephthalate (PET) plastic. Overall, PET has a massive application in different sectors of industry including synthetic fibers (clothing), food packaging, films, thermoforming implementations, and engineering resins.[15,16] Similar to other plastics, PET demand will see an annual increase of 3.5% globally and therefore, waste management traditions need to be modified and updated to be able to keep pace with the projected fabrication and consumption rates. Plastics are a useful reserve in many ways but plastic pollution is a waste of that valuable resource. In this work, we investigated the energy storage capability of upcycled Polyethylene Terephthalate (PET) plastic waste. The pristine upcycled material that was collected via fiberization and controlled carbonization, showed the combination of supercapacitive and pseudocapacitive behaviors. Next, by adding silicon nanoparticles and elemental sulfur, a composite Si-C anode and a S-C cathode were developed, respectively. Later, the generated electrodes were tested in half-cells in a lithium-ion battery setup.

1.2 Global Warming, Climate Change, and Energy Storage

Today, we know that climate change and global warming are disturbing the earth's ecosystems. To alleviate the extreme consequences, a reduction in greenhouse gas emissions and oil dependence is inevitable.[17–21] Rapid accumulation of CO_2 in the atmosphere disturbs nature's ability to consume it and puts the global carbon cycle off balance. This would increase the atmosphere's heat capacity and allow for maintaining more heat from the sun and subsequently raise the average temperature of the earth. It is predicted that the average temperature can see an increase of 2 °C - 11 °C by the end of this century.[22] This continuous increase in global average temperature could lead to a variety of possible effects listed below:

- Melting glaciers[23]
- Ocean acidification[24,25]

- Sea level rise[26,27]
- Extreme Weathers[27–30]

According to the Inventory of U.S. greenhouse gas emissions and sinks for the period of 1990-2019, since the industrial revolution (1750) there has been an 47% increase in global atmospheric concentrations of carbon dioxide (CO_2). Moreover, 80.2% of total greenhouse emissions is linked to CO_2 (Fig. 1.1). Specifically, for the period 1990-2019 a 3.1% increase in total emissions of CO_2, equivalent to 157.9 Million metric tons was observed. The main source of CO_2 emissions (92.7%) is fossil fuel combustion, mainly from transportation and power generation. In this respect, zero-emission Electric Vehicles (EVs) with a rechargeable battery show promise as a green and clean alternative.

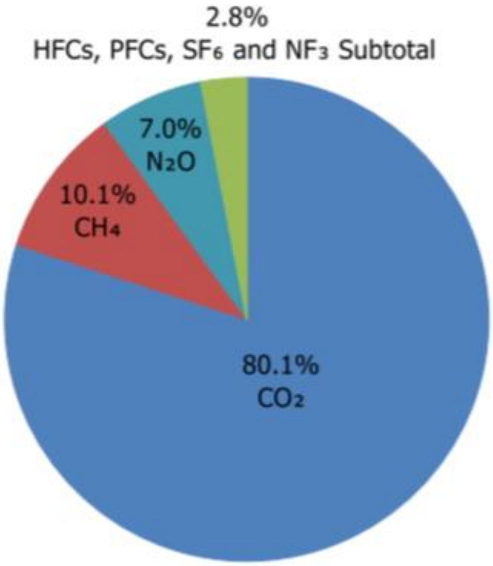

Fig.1.1 U.S. greenhouse gas Emissions by gas type (2019, Percentages based on MMT CO_2 equivalent)

1.3 Clean Energy and Energy Storage

To fight the severe effects of climate change and alleviate the global warming trends, a decrease in greenhouse gas emissions and dependency on fossil fuels is inevitable. Solar, wind, and hydroelectric dams are among clean and available energy alternatives, but they all suffer from a major drawback: sustainability. Their limitation to provide a steady energy and power at all times of the day is limiting their application. Moreover, the efficiency of each is highly dependent on sorting the harnessed energy in a system like a battery to be used when the sun is not shining and/or the wind is not blowing. To fill this gap, rechargeable batteries and supercapacitors are favorable. Batteries store the energy base of the Faradaic process that involves electron transfer through the redox reactions proceedings at the electrodes, while capacitors store the energy electrostatically, which is a non-Faradaic method whereby the charges are stored on two or more conductive plates separated by a dielectric barrier (separator).

1.4 Rechargeable Battery vs. Capacitor

When it comes to storing energy for electronics, rechargeable batteries and supercapacitors are the candidates. Batteries can store high amounts of energy in chemicals, but capacitors store the energy in an electric field. Rechargeable batteries such as lithium-ion, nickel-metal hydride, and lead-acid store chemical ions in the void spaces of the electrode structure or in terms of alloyed ions to the active material. Because of this, batteries own relatively high specific capacity (mAh g^{-1}), specific energy (Wh g^{-1}), and energy density (Wh L^{-1}). However, the required ion transportation that is necessary for transforming the chemical energy to electricity slows down the chemical reaction and thus the energy release. As a result, rechargeable batteries lack the ability to provide a high-power density (W g^{-1}) which is necessary for applications such as: accelerating EVs, power tools, applications requiring many rapid charge/discharge cycles, short-term energy storage, etc. In contrast, capacitors can release high amounts of energy in short bursts because they function by sorting the ions on the surface of the active material and therefore, they can release the energy much faster. However, because of a much lower surface area in comparison to rechargeable batteries, they can store lower amounts of energy. For instance, the flashbulb of a camera works with a supercapacitor where a fast release of high amounts of energy is required for a short period. However, the capacitor utilizes a battery with a much higher energy density for the recharge process. Supercapacitors can be classified as Electric Double-layer Capacitors (EDLC) and Pseudocapacitors. EDLCs are a class of parallel plate capacitors that store charge in an electric field at the interface between an electrolyte and a conductive electrode. At the interface, two rows of charge with opposite polarity will form: one on the electrode surface and the other electrolyte ions. Positive electrolyte ions are attracted to the negative plate, and negative electrolyte ions are attracted to the positive plate while there are no interactions between the electrode and the electrolyte ions. Pseudocapacitors fall between EDLCs and batteries where they can store much more energy than EDLCs and can charge/discharge much faster than a battery. Pseudocapacitors store energy faradaically by Pseudocapacity intercalation, electrosorption, and surface redox reactions. Since there is no phase transformation, the charge and discharge processes can be very fast.

1.5 Lithium-ion Batteries, Configuration and Principle

Among the secondary batteries, rechargeable Lithium-ion Batteries (LIBs) are very promising due to their high balanced energy density, very low internal resistance, low self-discharge rate, high cycle life, and good cycling capability. LIBs consist of a negative electrode (anode), a positive electrode (cathode), an electrolyte, and a separator which is usually a porous polymer membrane separating the two terminals from each other. The redox reactions happen at the electrode/electrolyte interface while the electrolyte provides a conductive environment facilitating the ion diffusion during the charge/discharge cycles. This is the main similarity that LIBs share with conventional batteries. In contrast to galvanic cells, there are heterogeneous oxidation-reduction reactions associated with LIBs that follow solid-state mass diffusion and volume expansion/contractions.[31] The schematic of a typical LIB is illustrated in figure 1.2. For a typical LIB, the anode is made of graphite, and the cathode is some sort of lithium metal oxide ($LiCoO_2$). Both electrodes have layered structures allowing the lithium ions to be stored in their voids. During the discharge process, lithium ions leave the anode, travel through the electrolyte and separator, and store in empty sites of the cathode. The reverse process happens during charge, where lithium ions migrate back to the anode and start alloying with graphite. At the same time, the involved electrons travel through the outer circuit, enabling us to use the current during the discharge period. The redox reactions at the electrodes are shown in equations 1.1 and 1.2:

$$C_6 + Li^+ + e^- \Leftrightarrow LiC_6 \text{ (anode)} \qquad (1.1)$$

$$CoO_2 + Li^+ + e^- \Leftrightarrow LiCoO_2 \text{ (cathode)} \qquad (1.2)$$

Being able to convert chemical energy to electricity with high efficiency and stability, LIBs can open new doors for storing the energy from the sun, wind, geothermal, hydroelectric, and other viable resources and become the primary source for energy storage.

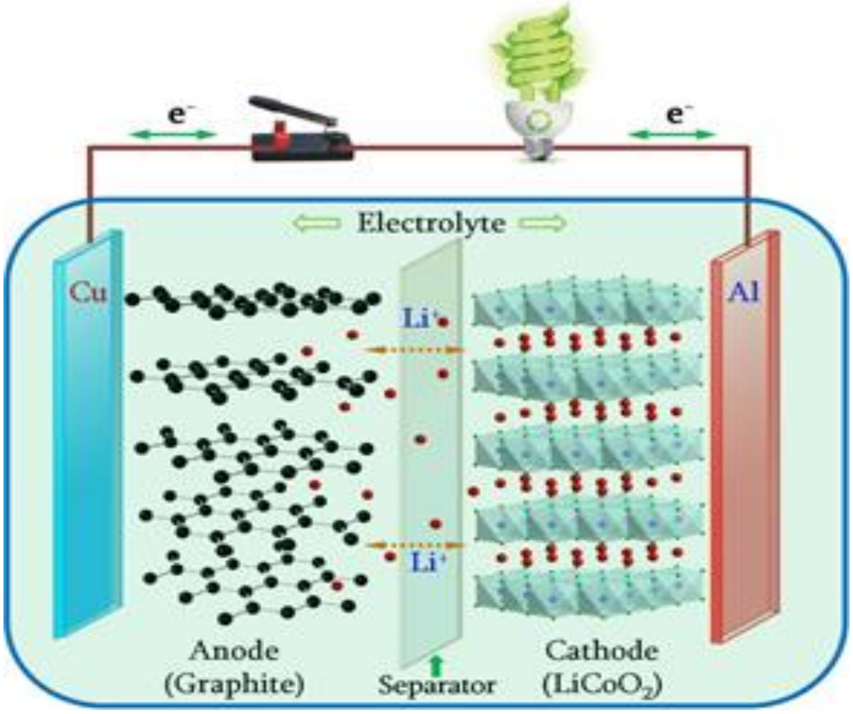

Fig. 1.2. Schematic representation of a conventional LIB configuration consisting of a graphite anode, $LiCoO_2$ cathode, a separator, and electrolyte. As illustrated in the figure, during the charge process Li-ions are pulled from the cathode through the electrolyte and across the separator to the graphite anode, where they are stored. The reverse process happens during the discharge and Li-ions move back to the cathode. In the half-cells, Li metal is used as the anode and Li-ions are extracted from the metal surface during the discharge.[32]

However, the specific capacity of current technology has reached its limits. Next-generation LIBs require more advanced and safe electrode materials with limited or controlled volume expansion/contractions that can provide high active material utilization and high capacity as well as being environmentally benign. In this regard, various attempts have been made to optimize the batteries performance including: i) electronic conductivity enhancement via engineered nano carbon materials[33,34], ii) nitrogen-doped carbon structures[35–37] iii) electrode and separator coating with conductive polymers[38–41], iv) electrolyte optimization and introducing additives[44–46] However, most of the advanced synthesis and optimization processes are very complex and costly and therefore, they are not applicable for mass production. In this work, PET plastic waste was used to generate nanofibers through an electrospinning process. Then the fibers went through controlled carbonization to yield microporous activated carbon. The obtained material had primary application as a supercapacitor and further, its application in anode and cathode active material modification was studied. All the production methods are widely used in industry with the advantages of being scalable, efficient, and cost-friendly.

1.6 LIB Anode Active Materials

New advancement in electric/hybrid vehicles and portable electronics has pushed the boundaries of their required energy density. In this regard, the very limited energy density of graphite (372 mAh g^{-1}, corresponding to LiC_6) cannot satisfy the rising energy demand of modern applications. In addition to its low capacity, graphite anode accounts for 24% of the production cost of a typical LIB.[47] Since graphite manufacturing is very energy exhausting and produces massive amounts of greenhouse emissions, researchers are exploring other environmentally friendly and abundant materials to achieve a higher energy density and specific capacity for the batteries. Although Li metal has the highest theoretical capacity as an active anode material, its employment is hindered due to its infinite volume expansion (dendrite formation). With continuous cycling, the ongoing growth of the dendrites leads to a low Coulombic efficiency as well as raising a safety concern with respect to a possible internal short circuit between the electrodes. Other viable anode candidates include Aluminum, Tin, and Silicon (Si). Among them, Si has gained a lot of attention due to its very high theoretical capacity of 3572 mAh g^{-1} (corresponding to $Li_{15}Si_4$ at room temperature), and having a low discharge potential of ~ 0.5 V against Li/Li^+ as well as being abundant, relatively inexpensive, and environmentally friendly. By using silicon, we can fabricate LIBs with lower weight, volume, and manufacturing cost while their energy density can be as high as 10 times that of graphite. But, this very high capacity comes at a cost: material pulverization and rapid capacity fade. Being able to host massive amounts of lithium ions, the electrode structure would expand during the charge process and shrink upon the discharge. These volume expansions/contractions can be up to 400% during the lithiation/delithiation processes which causes structural microcracks, leads to material degradation, and fast capacity loss. Moreover, silicon is not a good electronic conductive material, and it needs to be hosted by some sort of conductive agent. To mitigate these drawbacks, several approaches, including the introduction of Si nano structures, binders, and conductive agents are tested.[48–50]

1.7 LIB Cathode Active Materials

Analogous to anode materials, cathode active materials can host Li-ions via intercalation and deintercalation mechanisms during the discharge and charge processes. Today, the composition of the cathode is mainly constructed using transition metal oxides in different structures. The most frequently used compounds are Lithium Cobalt Oxide (LCO), Lithium Nickel Manganese Cobalt Oxide (NMC), Lithium Nickel Cobalt Aluminum Oxide (NCA), Lithium Iron Phosphate (LFP), and Lithium Manganese Oxide (LMO). The choice of the compound depends on different parameters, including operating temperature, cell voltage, capacity, energy density, and cycle life. Besides their relatively low capacity, these materials are not thermally stable, and they undergo rapid degradation that can cause thermal runaway and gas evolution that are significant safety concerns. Moreover, the release of oxygen atoms related to the phase change of the materials, accelerates the electrolyte decomposition and promotes a chain of unwanted side reactions. To overcome these challenges, researchers are devoted to finding better suited active materials with the benefit of being abundant and environmentally friendly as well as possessing a high energy density. Recently, Li-S batteries have gained a lot of attention because of their high theoretical specific capacity (1675 mAh g^{-1}, a magnitude larger than that of transition metal oxides). The high capacity is linked to sulfur's ability in accepting 2 electrons to be reduced to Lithium Sulfide (Li_2S). Moreover, sulfur is very abundant, cheap, and low in mass.[51–53] Li-S systems rely on the reversible reaction shown below:

$$2\,Li^{+} + 2\,e^{-} + x\,S \Leftrightarrow Li_2S_x \quad 1 < x < 8 \qquad (1.3)$$

The reaction advances using lithium Polysulfide (LiPS) intermediates that are soluble in the electrolyte and can migrate freely to the electrodes during the charge and discharge. The challenges regarding Li-S batteries are: i) insulating nature of lithium sulfides and elemental sulfur, ii) sulfur volume changes, iii) dissolution of LiPS in the electrolyte, iv) LiPS corrosion on Li anode at high currents, and v) Li dendrite formation on the Li anode.[54,55] To overcome these challenges, researchers have developed different approaches such as penetrating molten sulfur into different porous conductive carbon materials. Via this method, LiPS can be physically trapped, and an interconnected conducting network can be achieved. Examples of carbon materials used include micro- and meso-porous carbons, graphene, carbon nanotubes, etc.[56–60]

1.8 Electrochemistry Terms Used in This Dissertation

In order to understand the electrochemical analyses, the basic explanation of the electrochemical terms used in this study is provided in this section.

Capacity: is the amount of charge stored in an energy storage device, and it is dependent on the mass of the active material. In other words, capacity is the maximum amount of energy that can be extracted from a device during the discharge process. For a rechargeable battery, the rate of the charge/discharge is defined by the extent of the applied/withdrawn current, and it has a big impact on the capacity. Higher discharge rates are usually correlated with lower capacity as there is an optimum time needed for mass transfer and ionic transportation. Capacity is usually measured in either ampere-hours (Ah), watt-hours (Wh), or kilowatt-hours (kWh), while Ah is the most common for academic research. Since the voltage of the battery changes throughout the charge/discharge cycles, Ah is commonly used when studying the batteries. Under constant current cycling, the practical capacity of the battery can be calculated as the current multiplied by the elapsed time. Similarly, specific capacity is linked to the mass of the active material, and it is characterized as the capacity per mass of the active material (Ah g^{-1}). The theoretical specific capacity can be calculated using the Faraday's law shown in equation 1.4:

$$Q = nzF / M_W \qquad (1.4)$$

Where Q is the nominal capacity, n is the number of electrons involved in the redox reaction of 1 mol active material, z relates to the number of electrochemical species, F is Faraday's constant (96485 C mol^{-1}, or 26801 mAh mol^{-1}), and M_W is the molecular weight of the active material. For example, the theoretical capacity of Si (corresponding to $Li_{3.75}Si$) can be calculated as follows:

$Q_{Si} = 3.75 \times 1 \times 96485$ C/mol / 28.08 g/mol × 1000 mAh/3600 C = 3589 mAh g^{-1}

C-rate: defines the speed of charge/discharge cycles of a battery and it is the measurement of the applied current. For instance, 1C is related to the magnitude of a current needed to charge/discharge a battery in 1 hour. For example, a fully charged battery with a capacity of 20Ah can deliver 20 Amps for 1 hour. C-rates are calculated based on theoretical capacity using equation 1.5:

$$C\text{-}rate = Q / time \qquad (1.5)$$

Using the equation, 1C and 0.1C for a Si anode can be calculated as:

$$1\text{C} = 3589 \text{ mAh g}^{-1} / 1\text{h} = 3589 \text{ mA g}^{-1}$$

$$\text{C}/10 = 3589 \text{ mAh g}^{-1} / 10\text{h} = 358.9 \text{ mA g}^{-1}$$

Simply put, C/10 defines the current needed to fully charge/discharge a Si anode over 10 hours.

Coulombic Efficiency (CE): is used to characterize a secondary battery where it defines the charge transfer efficiency of the system. CE describes the loss of lithium ions during each cycle, and therefore, it is used to estimate the cycle life of the battery. CE has a direct relationship with battery efficiency, and thus, a high CE means longer life and better ionic/electronic transportation. CE is calculated using equation 1.6:

$$CE = Q_{Discharge} / Q_{Charge} \qquad (1.6)$$

where, $Q_{Discharge}$ is the capacity discharged and Q_{Charge} is the capacity charged. In other words, CE tracks the number of Li-ions involved in each charge/discharge cycle. A CE of 100% is translated to an ideal battery system in which during a complete cycle, 100% of the intercalated Li-ions during the discharge are migrated back to the anode upon charge or vice versa. However, different factors such as unwanted side reactions, heat generation, gas evolution, and electrodes structural degradation will lead to loss of Li and lowering the CE.

Internal Resistance (IR): is defined as the opposition to current flow in a battery. For LIBs, the overall internal resistance is due to electrolyte resistance, charge transfer resistance, mass transport resistance, and proceeding reactions at the electrolyte-electrode interface. Based on its origin, various IR sources develop at different time scales. The resistance associated with the electrolyte ionic mobility reacts rapidly to the applied current, thus this impedance happens at very fast time scales or at high frequencies. Charge transfer resistance relates to middle frequencies because it happens at a relatively longer time scale. Because mass transport occurs much slower, the associated resistance happens at low frequencies or the longest time scale. The overall IR can be calculated using equation 1.7:

$$R = V / I \qquad (1.7)$$

where, R is the resistance in ohms (Ω), V is the voltage in volts (V), and I is the current in amperes (A).

Chapter 2

Upcycling of Polyethylene Terephthalate (PET) Plastic Waste to a Carbon Energy Sorting Medium Through Electrospinning and Controlled Carbonization

In this chapter, the proceeding of upcycling PET plastic waste to a microporous carbon medium with principal application in supercapacitors is presented. The PET plastic waste went through dissolution, fiber production, controlled carbonization, and post-treatments and later its application for energy storage was evaluated. Various PET solutions with different nominal concentrations were tested, and the optimum solution was chosen to create ultrathin PET fibers via electrospinning technique. On the one hand, electrospinning is a very simple and scalable method with the ability to provide extremely long fibers that are very uniform in the diameter.[61,62] The mechanism of fiber production is based on the 1D stretch of PET solution, which is a result of electrostatic repulsion of surface charges.[63] Since the elongation of the polymer solution occurs via an external field and there is no physical contact in the process of fiber generation, electrospinning can lead to fibers with much thinner diameters.[64] on the other hand, because of being a continuous process, it can easily be used for mass production. For instance, because of its high efficiency, electrospun fibers have been used in the separation/filtration industry for more than 35 years.[65] Moreover, morphology and diameter of fibers can be controlled by varying one or more of the following: i) polymer type, ii) solvent type, iii) viscosity of the polymer solution, iv) strength of the applied electric field, v) the distance between the spinneret and collector plate, vi) feeding rate, vii) operation temperature and viii) chamber humidity level.[62,66]. In this chapter, we introduce a scalable synthesis of PET-derived activated carbon that has its primary application as a double-layer supercapacitor and can be further employed in electrode preparation of lithium-ion and non-lithium-ion energy storage devices. The material is microporous with a relatively high surface area and can be employed in various applications such as windmills, solar fields, grid energy storage, etc.

2.1 Methods and Materials

2.1.1 Fiber Production & Carbonization

By dissolving small pieces of PurAqua PET bottle in a solvent mixture of Trifluoroacetic Acid (TFA, Alfa Aesar, 99%) and Dichloromethane (DCM, Acros Organics, 99.9%, extra dry), a homogeneous 10 weight percent (wt.%) PET solution was prepared. The solvents ratio was 70 to 30 wt.% for TFA and DCM, respectively. To achieve a consistent distribution of the PET polymer in the solution, mechanical stirring was applied for 24 hours. PET nanofibers were collected by electrospinning technique (Inovenso NE300 electrospinning machinery). The applied voltage was around 19.0 kV while the feeding rate was held constant at 720 μLh^{-1}, and the chamber humidity was maintained around 40%. The spinneret and collector plate were 12 cm apart. All the parameters can be tuned to control the fiber density as well as the relative size and morphology. To generate a carbon network, the fibers were carbonized in a quartz tube furnace (MTI, OTF – 1200 X) using a mixture of Ar and H_2 gas. The gas mixture feeding rate was at 50 and 200 SCCM at 760 Torr for H_2 and Ar, respectively. To save the morphology and stabilize the fibers, the carbonization was carried out in 2 steps: first, with a heating rate of 5 °C min^{-1}, the temperature was raised to 220 °C (below the melting point of PET) and was held at this temperature for 2 hours; next, with the same ramping rate, the temperature was raised to the desired carbonization set point and was kept at that temperature for another 2 hours. To evaluate the temperature effect on the graphitization and defect density of the resultant materials, this process was done at 2 different final temperatures of 750 °C, and 1100 °C, and the as-prepared samples were named P750 and P1100, respectively. The carbonized samples were allowed to cool down overnight and were ball-milled prior to further use (MTI, MSK -SFM-1 machinery).

2.1.2 Material Characterization & Cell Assembly

Scanning Electron Microscopy (SEM) and Energy-Dispersive X-ray Spectroscopy (EDS) measurements were performed by a ThermoFisher Scientific, NNS450 instrument with In-lens SE/BSE detector (TLD). The electrospun fibers were platinum-coated using a sputtering machine before the SEM measurement. Raman spectroscopy was utilized to survey the composition of the electrospun fibers, as well as the content and graphitization degree of P750 and P1100. A Dilor XY Laser Raman with imaging microscope (Ar ion lasers and 532 nm Diode) was used. The X-Ray Diffraction (XRD) measurement was performed using a PANalytical Empyrean Series 2. Transmission Electron Microscopy (TEM) analysis was performed on a ThermoFisher Scientific, Tecnai12 with point and line resolution of 0.34 nm and 0.20 nm, respectively. Brunauer-Emmett-Teller (BET) measurement was carried out utilizing a volumetric instrument Micromeritics ASAP 2020. For the N_2 isotherm sorption, the sample was firstly activated at 200 °C and by evacuation (10^{-3} Torr) for 12 hours to remove gas and moisture before the measurement.

2.1.3 Cell Assembly & Electrochemical Measurements

For electrode preparation, the active material (P750) was mixed with the binder Polytetrafluoroethylene (PTFE) and acetylene black, with the ratio of 80:10:10 wt.%, respectively. The slurry solvent was N-Methyl-2-pyrrolidone (NMP), and its amount was equal to 2.01 wt.% of the binder. After the solvent addition, the slurry was mechanically stirred for at least 24 hours to reach the desired properties suitable for casting. By using a doctor blade, the slurry was cast on a Ni foam and allowed to dry overnight at 100°C in a conventional oven. Next, the casted slurry was calendared to the thickness of 0.30 mm before punching and assembly in a coin-type cell (CR2032, MTI). A symmetrical cell was constructed using 6.0 M KOH (aq) (Fisher Chemical) as the electrolyte. Both electrodes and the separator (Celgard 25um 3501) were submerged in the electrolyte solution overnight. A Bio-Logic testing module (BCS 810) was used to perform the electrochemical analyses. Cyclic voltammetry (CV) analysis was performed within the range of 0-1 V at the scan rates of 1, 10, 20, 40, and 100 mV S^{-1}. Galvanostatic Cycling with Potential Limitations (GCPL) was carried out under Constant Current (CC) cycling of 5, 10, and 15 mA. Electrochemical Impedance Spectroscopy (EIS) was conducted at the frequency window of 10 MHz to 10 mHz with a perturbation signal of 10 mV. EIS was performed at the end of the first cycle and followed every 1000 cycles to track the impedance alteration throughout the long-term cycling. Next, the data were fitted by a comprehensive equivalent circuit proposed in figure 2.9g.

2.2 Results and Discussion

2.2.1 Analytical Characterization

The development of nanofibers was affirmed by SEM images (Fig. 2.1) and Raman analysis (Fig. 2.2). The dual TFA-DCM solvent was chosen based on the solubility-spinnability map of PET, constructed using the ternary fractional parameters: polarity, dispersion forces, and hydrogen bonding.[67] The polymer's solubility ability influences the solution viscoelasticity and fiber size as well as the aspect ratio and morphology of the fibers and therefore implies a very important effect on a bead-free and smooth nanofiber formation. The solvent evaporates while traveling to the collector plate, where the fiber jets can solidify to create PET nanofibers. Very high vapor pressure of the solvent system would allow its recovery via process-coupled condensation units on an industrial level.

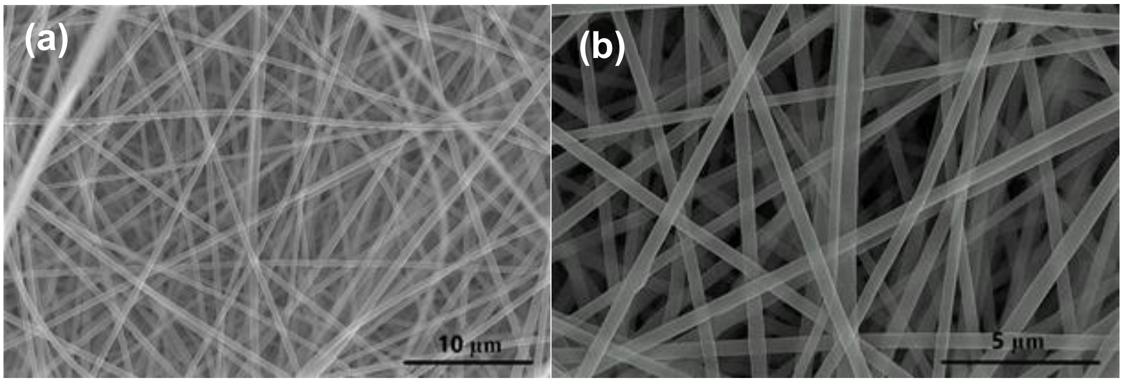

Figure 2.1. SEM images of an electrospun PET solution magnified to (a) 500x, and (b) 10,000x. The formation of a dense forest of PET fibers is observed.

From the SEM images, we observed a concentrated forest of smooth nanofibers with relatively uniform shape and diameter (the fibers diameter ranged from 100 nm - 0.80 µm).

The Raman profiles of the fibers, as well as the pyrolyzed samples, are provided in Figure 2.2. Because Raman spectroscopy is most sensitive toward carbon-carbon covalent bonds, it is highly reliable for studying carbon structures.[68–70] The Raman spectra of PET nanofibers (Fig. 2.2a) is a good match to the Raman spectra of unprocessed PET that suggest the following: the fibers are solvent-free, and the dissolution process is nondestructive.[71,72]

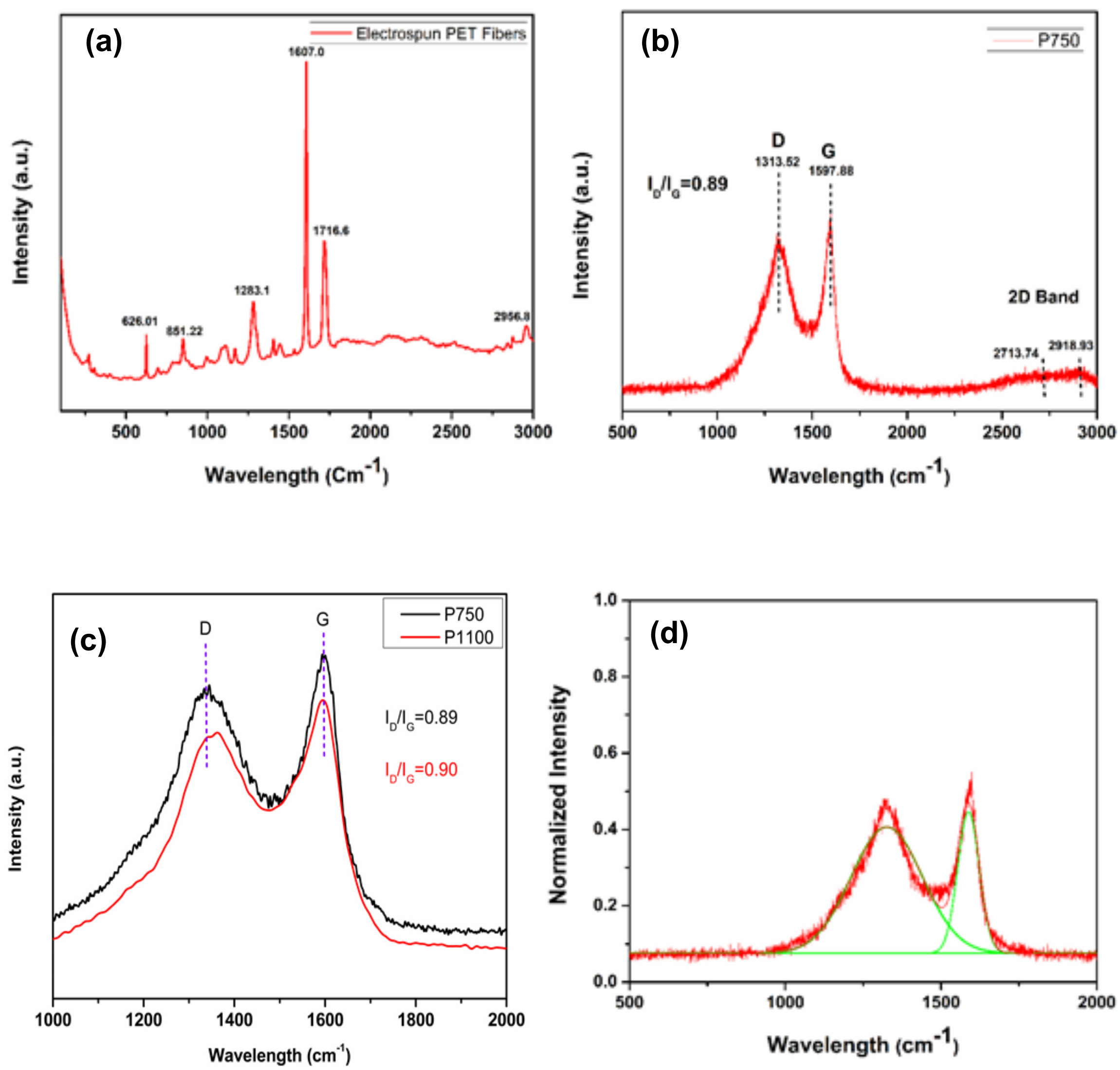

Figure 2.2. Raman spectra of the: (a) electrospun PET fibers before carbonization, (b) milled P750, after pyrolysis, and (c) milled P750 and P1100. (d) Lorentzian curve-fitting data of P750 expressing the absence of overlapped peaks.

Raman profile of P750 consists of 2 major peaks at 1313 cm^{-1} (D band) and 1597 cm^{-1} (G band). The D peak is related to structural defects that are caused by disordered conformation of graphene layers and further, it is ascribed to out-of-plane vibrations of carbon atoms with dangling bonds.[73,74] G peak is related to graphitic carbon structures with high order and is caused by in-plane vibration modes of aromaticity bonded carbon (C=C, sp^2 bonded).[74,75] Moreover, a semi-broad 2D band with local peaks centered at 2713 cm^{-1} and 2918 cm^{-1} was noticed. The 2D band is generally associated with reduced Graphene Oxide (rGO). Since the position and the intensity of the 2D peak is highly dependent on the stacking properties of the graphene layers, it can be applied to address the structure of the graphene sheets (mono, double, or multi-layer).[76-78] Because P750 showed a low 2D intensity and considering the peak position, we summarized that rGo is contributing to the signal.[78] The presence of multiple O groups can create voids and disturb the easy stacking of the graphene sheets and increase the material amorphicity that can cause a shift in the wavenumber. Another measure that can assist with graphitization degree determination is the R-value (I_D/I_G ratio). It is well understood that the R-value is highly dependent on the ratio of graphitic edge planes to normal graphite planes. The R-value of 0.89 is suggestive of high defects and low graphitic property of the material, similar to other reports on rGO.[77]

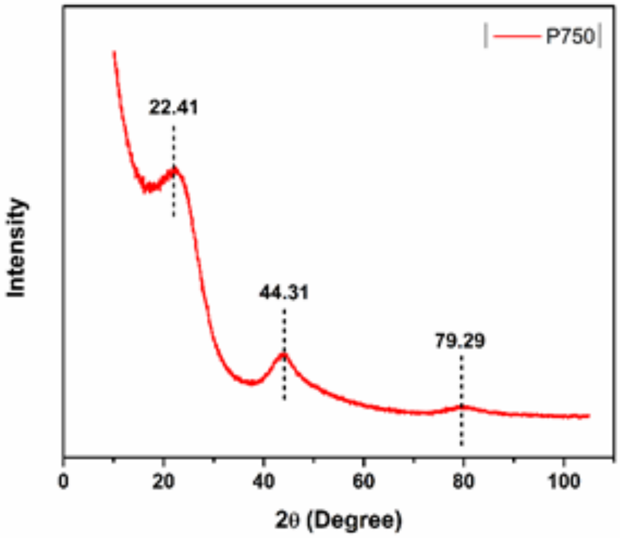

Figure 2.3. XRD pattern of P750 powder showing the peaks at 22.41°, 44.31°, and 79.29° that are characteristics of amorphous carbon and rGO.

For P1100 the R-value was equal to 0.90, which suggest a lower defect and higher graphitization degree of the material in comparison to P750 (Fig. 2.2c).

The XRD profile of P750 is shown in figure 2.3. From the graph, the peak at 22.41° with an interlayer spacing of 0.396 nm is related to graphitic structures. The peak quasi-broad shape and position are characteristic of amorphous Carbon (aC)and rGO.[79–82] The second and third peaks at 44.31° and 79.29° with relative interlayer spacings of 0.204 nm and 0.120 nm are corresponding to rGO, and they are in good agreement with our Raman analysis. The SEM, EDS, and elemental analysis of P750 are exhibited in figure 2.4. The EDS mapping data shows contributions from carbon, oxygen, and silicon. Normalized elemental quantification shows that the surface chemistry is mainly carbon. Silicon traces are due to the carbonization in a quartz tube furnace where silicon dioxide sublimes at the higher temperatures. rGO and silica are contributing to the oxygen content.

The high-resolution bright-field TEM images of P750 are shown in figure 2.5. From the images b-c, the presence of ordered graphitic structure domains that are spread out throughout the mainly amorphous structure was observed. The Selected Area Electron Diffraction (SAED) pattern of P750 is also consistent with amorphous characteristics, and it is in excellent agreement with our Raman and XRD analyses.

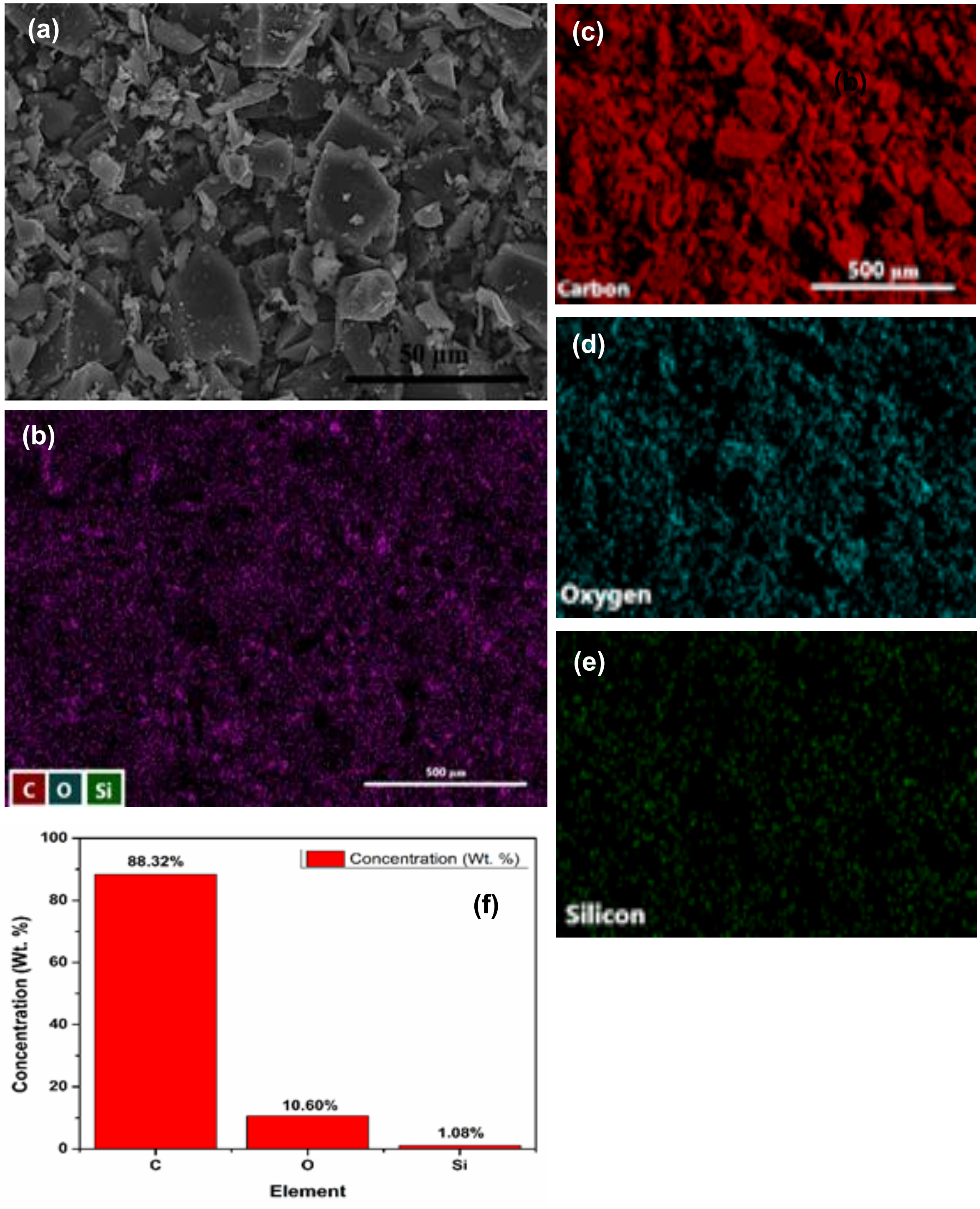

Figure 2.4. (a) SEM image of P750 after pyrolysis, (b) EDS mapping of P750 confirming the presence of C, O and Si. EDS mapping of (c) Carbon, (d) Oxygen, and (e) Silicon elements. (f) Corresponding elemental concentration analysis derived from EDS data.

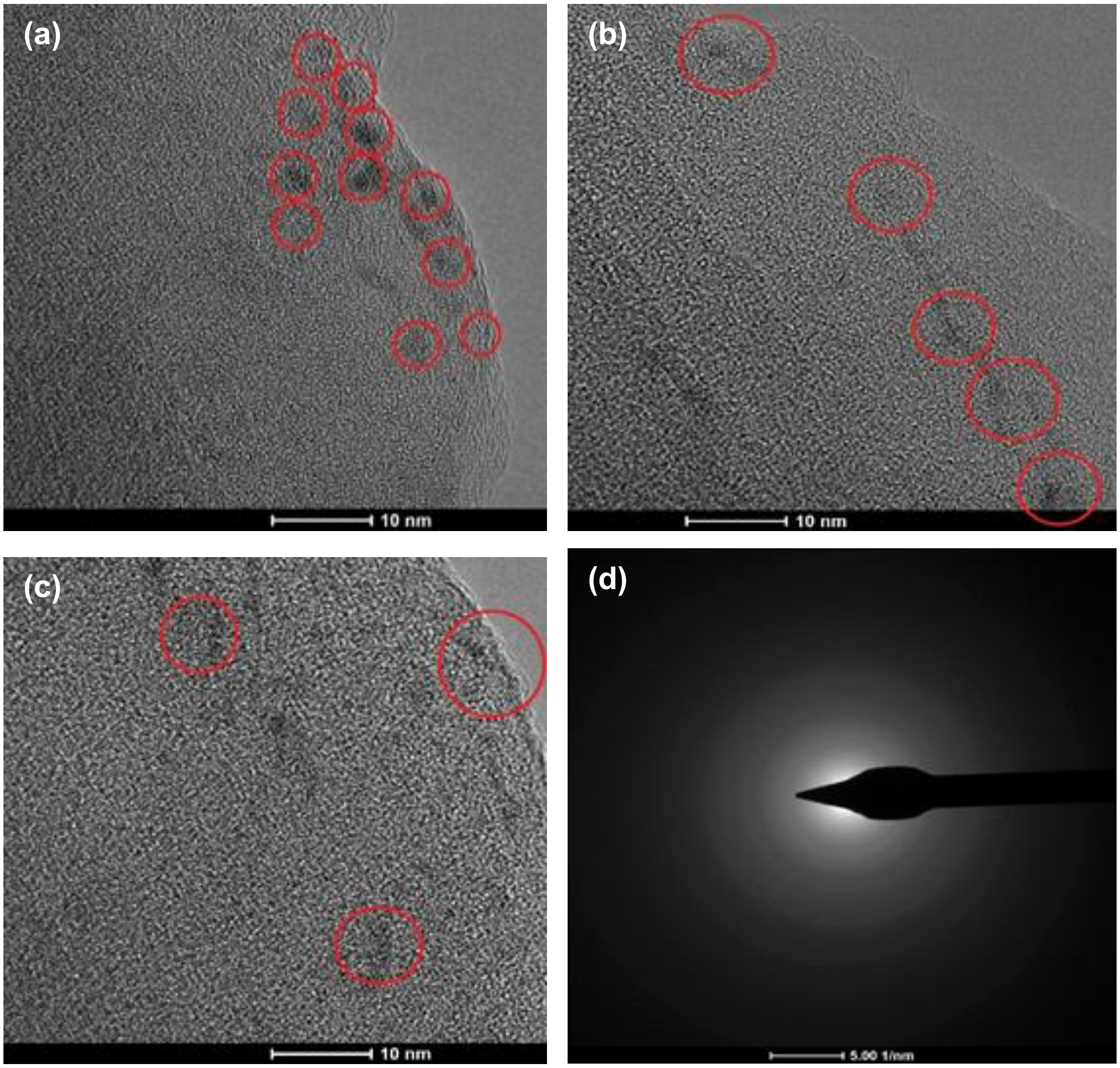

Figure 2.5. TEM images of P750 showing the degree of crystallinity in the sample. Panels (a-c) show the presence of ordered domains that are in excellent agreement with Raman and XRD analysis. The selected area electron diffraction (SAED) pattern (d) is also consistent with amorphous carbons.

Based on our findings we summarized the following: i) the carbon network is mostly predominated by the amorphous structure, and ii) the sample might consist of mostly sp^2 sites without a long-range order. The TEM images of P1100 are displayed in figure 2.6 below:

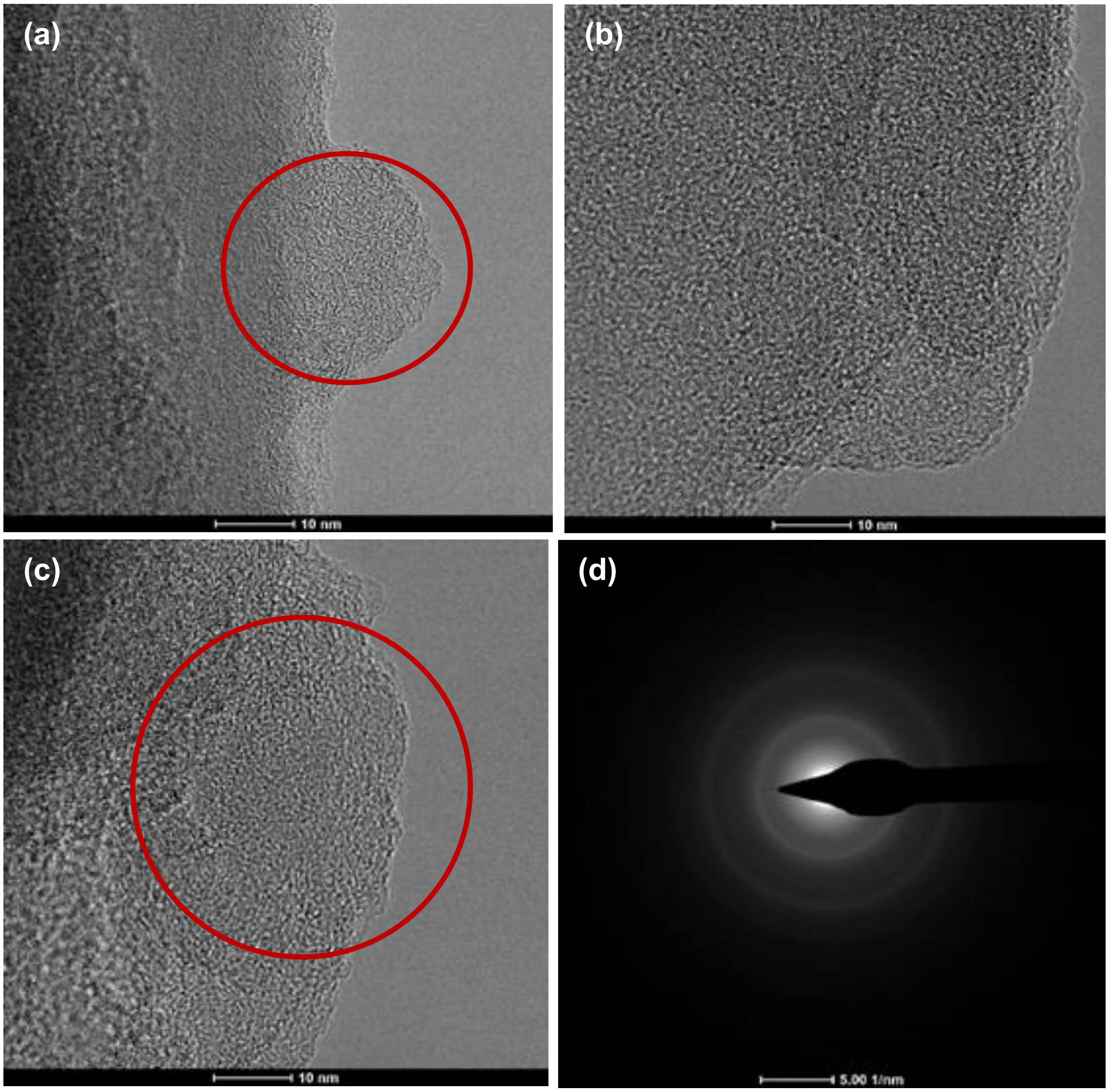

Figure 2.6. TEM images of P1100 showing the increased degree of crystallinity in the sample. Panels (a-c) show an increase in the size and prevalence of ordered domains. The selected area electron diffraction (SAED) pattern (d) shows the higher degree of crystallinity.

The carbonized samples at 1100 °C exhibit more random crystallinity compared to P750, and further, more ordered graphitic structures are noted. The material is turbostratic carbon as the graphene sheets are not properly stacked atop one another; Simply put, the sheets are haphazardly folded or crumbled but are still good for conduction. The SAED pattern is also in good agreement with turbostratic carbon. The nitrogen adsorption/desorption isotherms and the pore size distribution of P750 are displayed in figure 2.7. BET analysis revealed a microporous carbon structure with pore size and surface area of 4.65 Å and 456.6 m² g^{-1}, respectively. The pore size distribution was between 4.65 Å to 21.62 Å, concentrating at ~ 5.89 Å.

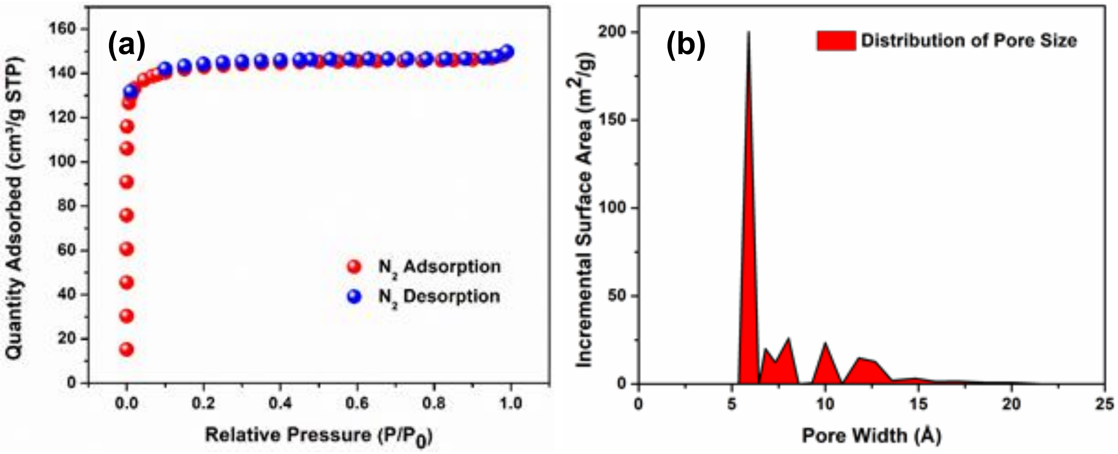

Figure 2.7. (a) N_2 sorption isotherm, and (b) relative pore volume distribution of P750.

Pore generation happens during the carbonization process when the excess heat generates vigorous atomic vibrations and causes pyrolization of the benzene ring, which is accompanied by partial oxygen removal. Oxygen departure and the decomposition of the organic linkers develop the detected micropores that can provide ample space for the electrolyte penetration (water-based electrolyte, water molecule diameter: 2.75 Å). Our analytical findings will be further supported by the electrochemical analysis discussed in the next section.

2.2.2 Electrochemical Characterization

Because P750 showed better electrochemical behavior in comparison to P1100, the electrode preparation, cell assembly, and electrochemical characterization were performed utilizing P750 as the active material. We surveyed the reaction kinetics of the material via CV, and the resulting profile is shown in figure 2.8a.

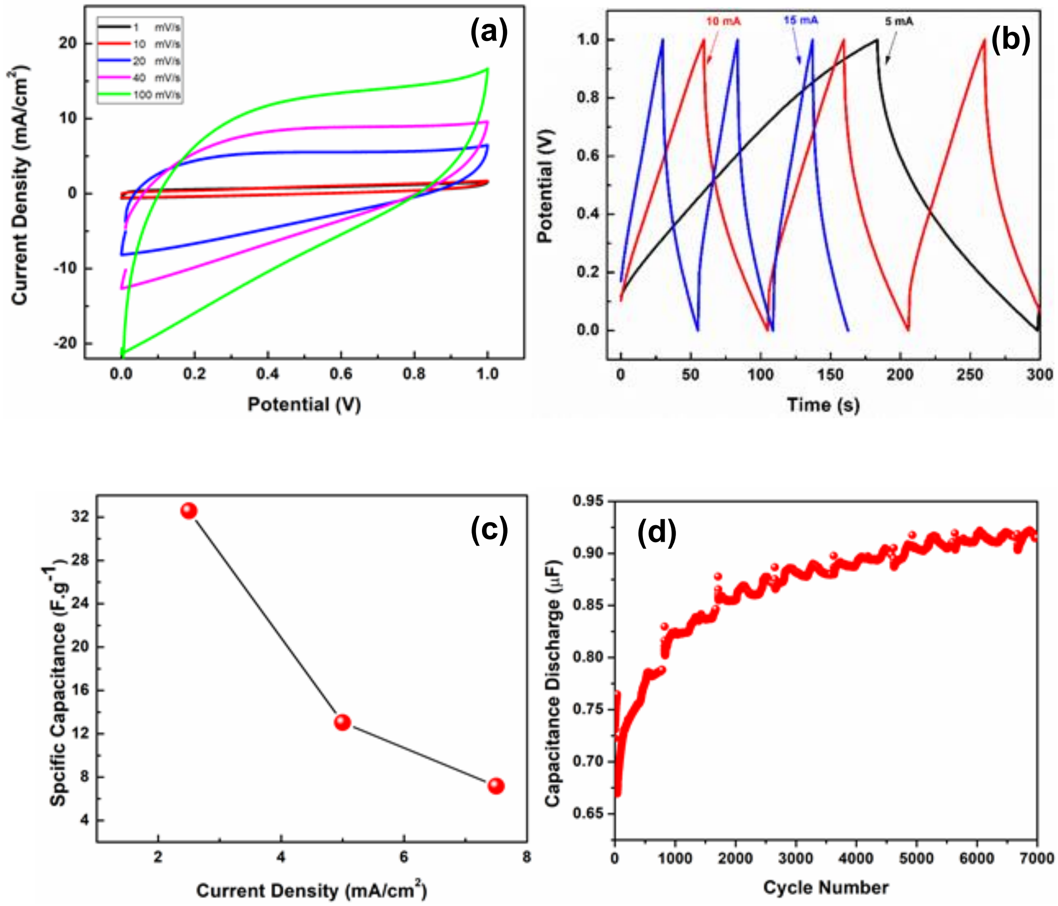

Figure 2.8. (a) Cyclic Voltammetry at scan rates of 1 mV/s, 10 mV/s, 20 mV/s, 40 mV/s, and 100 mV/s; (b) GCPL cycling performance of the supercapacitor under various current rates; (c) Specific capacitance under various current rates; and (d) long-term specific capacitance retention under 5 mA rate.

From the CV, the quasi-rectangular shape of the plots is indicative of double-layer capacitance in addition to redox reaction pseudo-capacitance and the absence of redox peaks suggest good capacitive behavior for P750.[83,84] The shape of the CV curves are very similar to a previously reported study for rGO that can add to our analytical findings.[85] The specific capacitance plot was obtained from the cycling data under different cycling rates (Fig. 2.8c). From the image, the quasi-linear and symmetric behavior of the charge/discharge cycles implies that redox pseudocapacitance and double-layer capacitance are contributing to the overall capacitance. The reported capacitance was determined using the equation 2.1:

$$C = 2*i/m(dV/dt) \qquad (2.1)$$

Where, i is the cycling current, m is the mass of the electrode, and dV/dt is the slope of the charge/discharge curve. The highest capacitance of 32.6 F. g^{-1} under 2.5 mA cm^{-2} constant current cycling rate was reached. The capacitance retention study of the material showed an increase of 126.7% in capacitance with continuous cycling up to the cycle 7000th. This ongoing capacity improvement is associated with the activation of the active material, which is related to the following: i) potential promoted activation of the material, ii) possible reduction in agglomerated sites, iii) an increase in the effective contact area, and iv) continuous penetration of the electrolyte through the micropores which lead to further wetting of the electrode structure.[86,87] To track the internal resistance alteration with prolonged cycling, EIS analysis was performed. The acquired experimental and fitted Nyquist profiles of the first, 2000th, 5000th, and 7000th are shown in figure 2.9. The proposed equivalent circuit in figure 2.9g describes the electrochemical features of the phases and interfaces. Equivalent Series Resistance (ESR) or R_S, is the sum of the electrodes internal resistance plus the electrolyte resistance. R_{CT} relates to the rate of redox reactions at the electrode/electrolyte interface. For the non-ideal capacitive performance associated with a non-uniform interface, a Constant Phase Element (CPE) was used. CPE_{DL} is related to the double layers: electrolyte ions and electronic charges at the interface.[88] The Warburg element (W_O) is related to the long tail of the Nyquist plot which lies in the intermediate and low-frequency zones. W_O is corresponding to the diffusion behavior of the porous material. R_L, is the leakage resistance with usually a large value. In parallel to R_L, CPE_L stands for the voltage-dependent pseudocapacitance of the redox reactions.[89] Table 2.1 summarizes the data of the first and 7000th cycles. From the Nyquist plots, the diffusion tail's slope against the real axis is about 45 degrees. However, for an ideal EDLC the angle is about 90 degrees.[90] This dissimilarity is mainly because of the induced pseudocapacitive behavior of the material due to the presence of the oxygen-containing functional groups on the surface.[91] From the image (2.9e), the capacity stays invariant against the frequency for a wide window that suggests decent supercapacitive nature of the material.

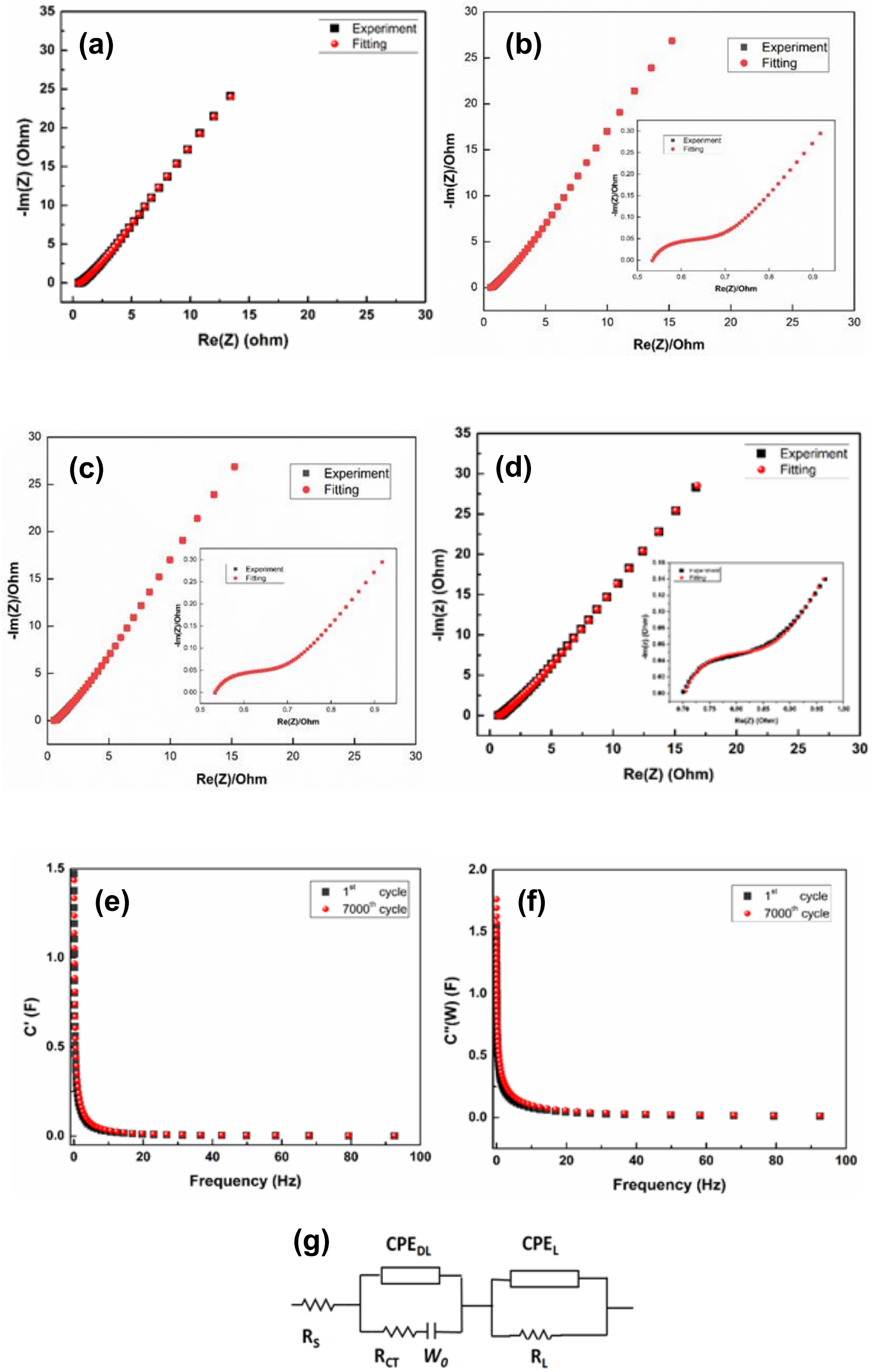

Figure 2.9. Nyquist plots of the experimental and fitting data at (a) 1st cycle, (b) 2000th cycle, (c) 5000th cycle, (d) 7000th cycle; (e) Real capacitance against frequency plot; (f) Imaginary capacitance against frequency plot; (g) Equivalent circuit to fit EIS data. The inlays represent the data of the first 50 cycles.

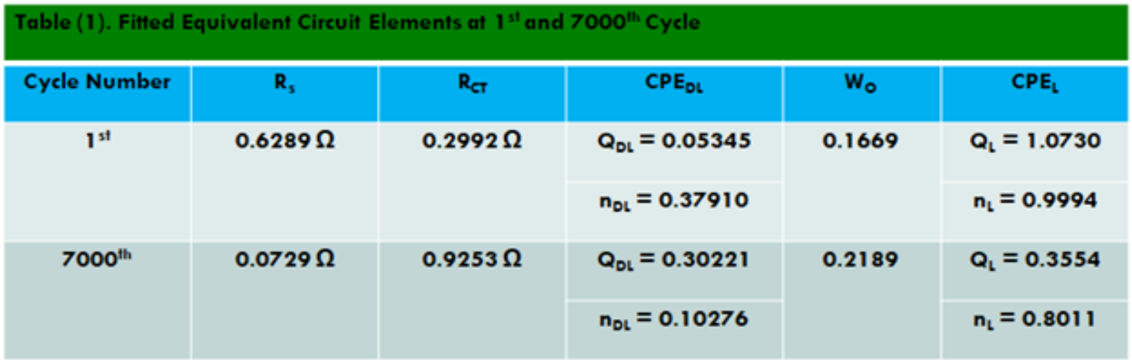

Table (1). Fitted Equivalent Circuit Elements at 1^{st} and 7000^{th} Cycle

Cycle Number	R_s	R_{CT}	CPE_{DL}	W_O	CPE_L
1^{st}	0.6289 Ω	0.2992 Ω	$Q_{DL} = 0.05345$	0.1669	$Q_L = 1.0730$
			$n_{DL} = 0.37910$		$n_L = 0.9994$
7000^{th}	0.0729 Ω	0.9253 Ω	$Q_{DL} = 0.30221$	0.2189	$Q_L = 0.3554$
			$n_{DL} = 0.10276$		$n_L = 0.8011$

Table 2.1. Fitted equivalent circuit elements at first and 7000th cycle for P750.

The relatively huge decrease of the internal resistance (R_S) is mainly related to the continuous material activation via further electrolyte penetration into the electrodes' structure. This observation is in line with the detected increase in capacitance with prolonged cycling. In addition, the electrolyte resistance is low because the aqueous medium is highly conductive and facilitates rapid charge transfer. On the other hand, the observed increase of R_{CT} and CPE_{DL} values can be assigned to the following: i) it has been reported that pore size can manipulate the ionic and electronic conductivity, and therefore, has an important influence on the charge transfer resistance of EDLC electrodes.[92] Because of the wide pore size distribution of P750 (4.65 Å to 21.62 Å, mostly below 10 Å), nonuniform utilization of the active material can lead to an increase in R_{CT}. ii) The graphitization degree and morphology are the other factors impacting the charge transfer kinetics. In this sense, by continuous activation of the mainly amorphous carbon material, the electrode's operational area and R_{CT} would increase. This experience can be further explained by the ideal factor, n_{DL}. n_{DL} which ranges from 0 to 1, corresponds to the homogeneity of the ionic and electronic double-layers at the electrode/electrolyte interface, where 1 presents a homogeneous and uniform interface and 0 corresponds to a nonuniform terminal. The detected decrease of the ideal factor (from 0.379 to 0.103) calls for a drop in the interfacial uniformity that can be related to an increase in defects and disorder density upon the activation of new sites. CPE_{DL} is solely related to the non-ideal double-layer capacitance, making it following the same increasing trend that was observed for the capacitance with long-term cycling. W_O explains the ion diffusion feasibility at the interface and corresponds to the pore size and surface area of the porous electrode. The noticed increase of W_O indicates harder electrolyte diffusion at the interface that can be related to the passivation of the interfacial pores, and introduction of new pathways upon further material activation. The noticed reduction in $CPEL_L$ value is due to the redox sites passivation with prolonged cycling. In summary, EIS analysis revealed that the material had combined the characteristics of EDLC and pseudocapacitors and material activation is an ongoing process with the help of the applied potential.

2.3 Application of PET-derived Carbon as an Anode Material for Lithium-ion Batteries

In this section, the employment of the generated carbon medium as an anode active material in a LIB setup is investigated. Since graphite manufacturing is a very energy-exhausting process with massive greenhouse gas emissions, producing a waste-derived carbon material that can compete with graphite performance is very interesting. The pipeline and details of the synthesis procedure will be discussed, and the data of the better performing proceeding will be highlighted. In addition, a comparison of the performance data will be presented.

2.3.1 Methods and Materials

Various PET solutions with nominal PET loadings of 5, 10, 15, 20, and 30 wt.% were developed. The solvents were TFA and DCM with the ratio of 70 to 30 wt.%, respectively. The samples went through an electrospinning process to develop very thin PET fibers. The electrospinning was carried out at different feeding rates, humidity levels, and voltages to understand the association of each parameter and find the optimum parameters suited for nanofiber generation. We found out that the solution viscosity and chamber humidity level play a crucial role in the development of smooth and bead-free fibers. Since the solvents have a very high vapor pressure, very viscose solution will rapidly solidify at the spinneret, and the ongoing agglomeration will result in formation of non-uniform and micro-milli fibers. In this regard, the 10 wt.% solution showed the best stability for long-term spraying with minimum condensation at the spinneret. Moreover, the chamber humidity level has a significant influence on the fiber formation via facilitating electric conduction between the spinneret and the collector plate. The humidity level of ~40% was sufficient to reach the desired fiber morphology in accordance with our desired feeding rate and provided voltage (720 μL h^{-1} and 19 kV). The feeding rate and provided voltage were also subject to the experimental examination but can be varied to better suit the desired requirements. The carbonization was carried out in a quartz tube furnace in the mixture of Ar and H_2 gas. This process was done in 2 steps: first, to stabilize the fibers, the temperature was raised to 220 °C with a heating rate of 5 °C min^{-1} and was held at this temperature for 2 hours; next, with the same ramping rate, the temperature was raised to 750 and 1100 °C and was kept at this temperature for 2 hours to investigate the temperature effect on the graphitization degree and cell performance. Because PET is an oxygen-rich material, the introduction of hydrogen gas is required to sufficiently reduce the graphene oxide sheets and provide a better-interconnected carbon network. The presence of oxygen functional groups can inhibit facile stacking of graphene layers and subsequently increase the network's defects density. The samples that were carbonized in the Ar atmosphere were a combination of amorphous carbon and graphene oxide, which is not a good energy sorting material. For the 10 wt.% sample, the calculated carbonization yield was equal to 24%. To remove the trace metal contamination and purify the carbonized sample, some samples were acid-washed using HCl at 80 °C, while a few samples were treated with KOH solution. Next, the samples were washed with DI water four times, followed by an additional washing step with ethanol twice. The samples were centrifuged at the end of each step (at 4000 RPM for 20 minutes) and prior to vacuum drying at 65 °C overnight. For cell assembly, different groups were modified to track the influence of the binder and carbon black on the performance of the cells. One group was constructed using the active material and binder (PVDF) with the ratio of 85:1 wt.%, respectively. Another group was made using the active material, binder, and carbon black with the ratio of 80:15:5 wt.%, respectively. As a reference, group 3 was carbonized PET bottle (without dissolution and electrospinning). It is worth noting that PAA was also tested as the binder for the anode development. However, the obtained cell performance was inferior in comparison to

PVDF, and therefore, PVDF binder was selected for future cell constructions. The active material, binder, and carbon black were hand-mixed using a mortar and pestle for about 10 minutes to make sure of uniform physical mixing of the materials. Next, with the addition of NMP solvent, a slurry was prepared and was mechanically stirred overnight to reach the desired uniformity suitable for casting. The slurry was hand cast on a copper foil and dried overnight at 100 °C in a conventional oven. Cell assembly was performed in an Ar filled glovebox with H_2O and O_2 levels below 1 ppm. The electrolyte was 1M $LiPF_6$ in a mixture of EC/DMC (ethylene carbonate and dimethyl carbonate= 50/50 (v/v)). The constructed cells were conditioned at C/40 for 3 cycles and later were subject to cycling at different C-rates (C/20, C/10, C/5, and 1C).

2.3.2 Results & Discussion

The assembled batteries were conditioned at a C/40 rate to allow for initial material activation as well as constructing a stable SEI layer. Figure 2.10 summarizes the average data from the conditioning cycles and C/5 (5 hours charge and 5 hours discharge) data. From the graph, it is seen that samples have a much higher capacity when cycled at a low cycling rate. The trend is typical for LIBs, and it is due to chemical mechanisms of degradation associated with capacity loss at low c-rates, whereas mechanical-induced mechanisms linked to higher current dominate at a higher c-rate. SEI formation and growth is unwanted because it results in lithium inventory loss. We noticed that P1100 did not show capacity improvements in comparison to P750. In general, because of the distorted configuration of turbostratic carbon, the carbon atoms are not completely interconnected, and because of that, even though the graphitization degree is higher, a better capacity contribution was not observed. The acid washed samples showed the worst performance, indicating that possible heavy metal contamination is not responsible for capacity loss and fading mechanisms. KOH treated samples did not display meaningful improvements either. From the graphs the highest efficiency was ascribed to P750 and therefore we continued to process our samples at this temperature. For instance, P750 showed the average C/40 specific capacity of 365 mAh g^{-1}, average C/10 specific capacity of 176 mAh g^{-1}, and average C/5 specific capacity of 162 mAh g^{-1} after 133 cycles. Figure 2.11 exhibits the cells' efficiency and rate capability at different c-rates of C/20, C/10, C/5, and 1C. As expected, with an increase in cycling current, a reduction in the reversible capacity of the cell was noticed.

Figure 2.11a displays a comparison between the cells, where the data is in the order of the C/5 cycling performance. C/40 data is also provided for the reader. It is worth noting that the provided data is the average value of the cells retrieved from the cycling data. C/40 values do not include the data of the first conditioning cycle to eliminate the Li usage associated with SEI formation. According to data, P750 shows the highest reversible capacity followed by P1100 with the addition of 5 wt.% carbon black. Acid and base treatments of the samples did not contribute to performance improvements, and P750 seems to be less affected by our post-processing. Figure 2.11b, presents the cycling capability of P750, P1100, and the post processed samples.

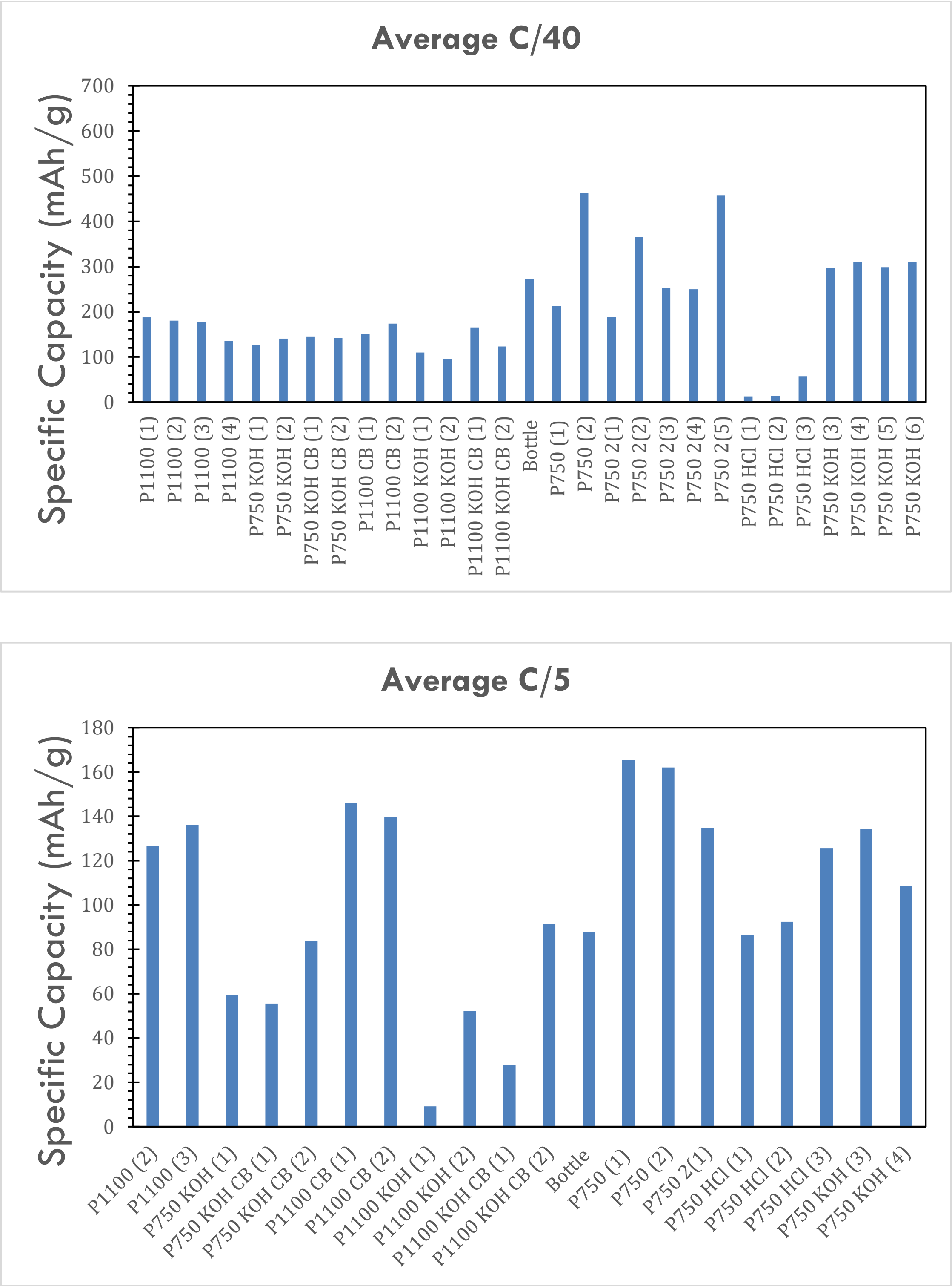

Figure 2.10. The average specific capacity of the cells at (a) C/40 CC cycling, and (b) C/5 CC cycling data. CB = 5 wt.% carbon black, bottle = untreated PET bottle that went through carbonization at 750 °C.

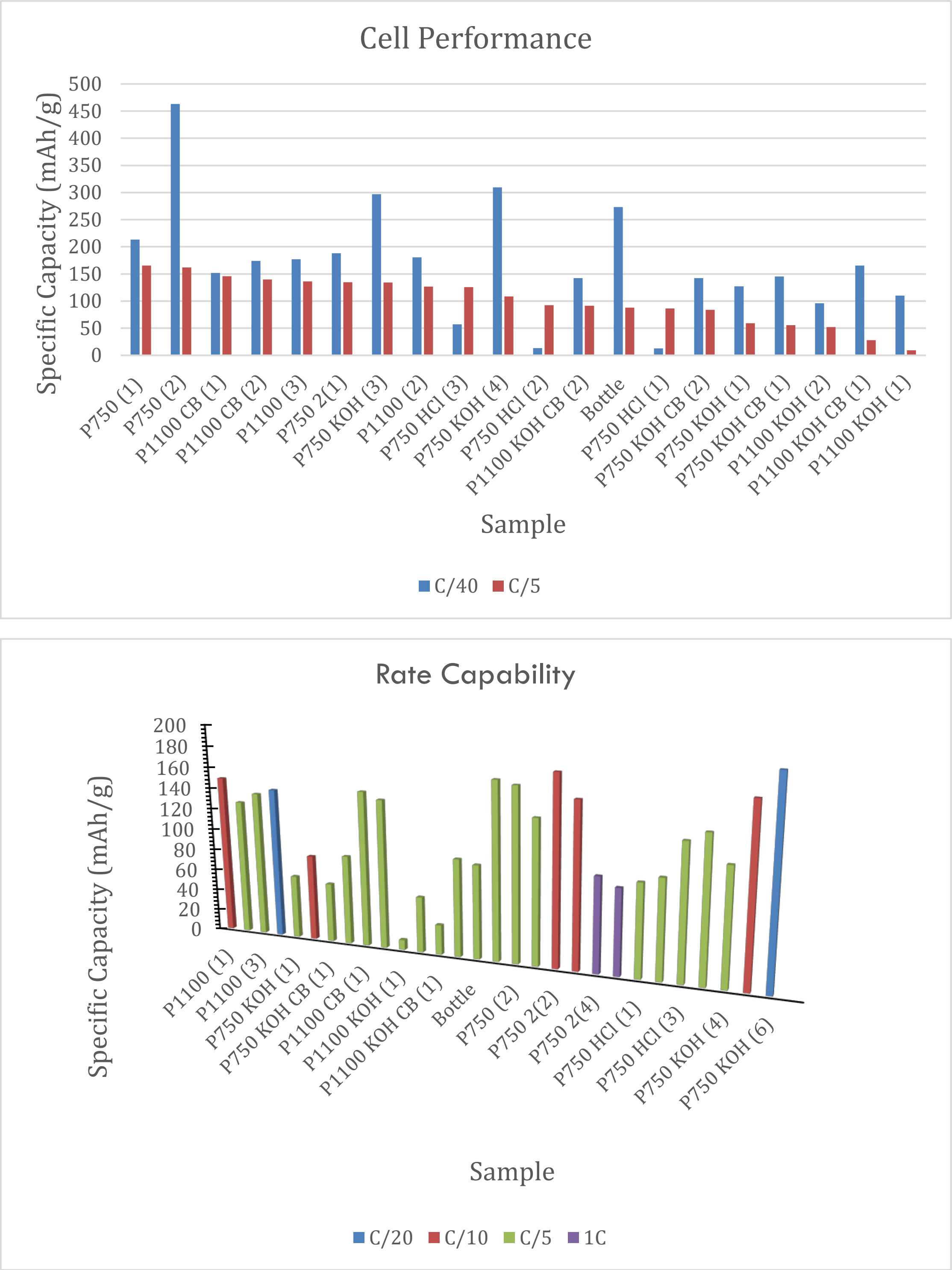

Figure 2.11. (a) Cell efficiency and (b) Rate capability of constructed cells via different carbonization temperature and post treatments. CB = 5 wt.% carbon black, bottle = untreated PET bottle that went through direct carbonization at 750 °C.

The CV profile of P750 presented in figure 2.12 is consistent with microporous carbon structures. The CV was conducted at extended voltage window to survey the possible capacity contribution of P750 at higher voltage ranges.

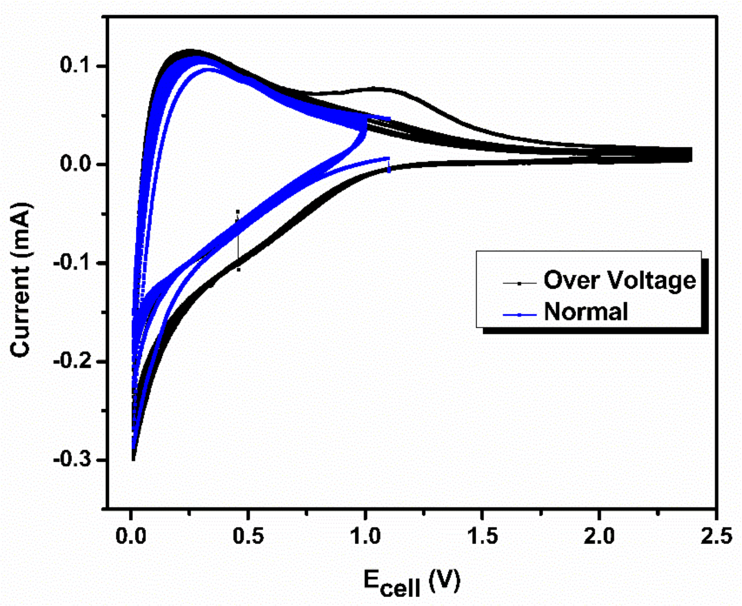

Figure 2.12. CV profiles of P750 at different voltage ranges of 0-1 V and 0-2.5 V.

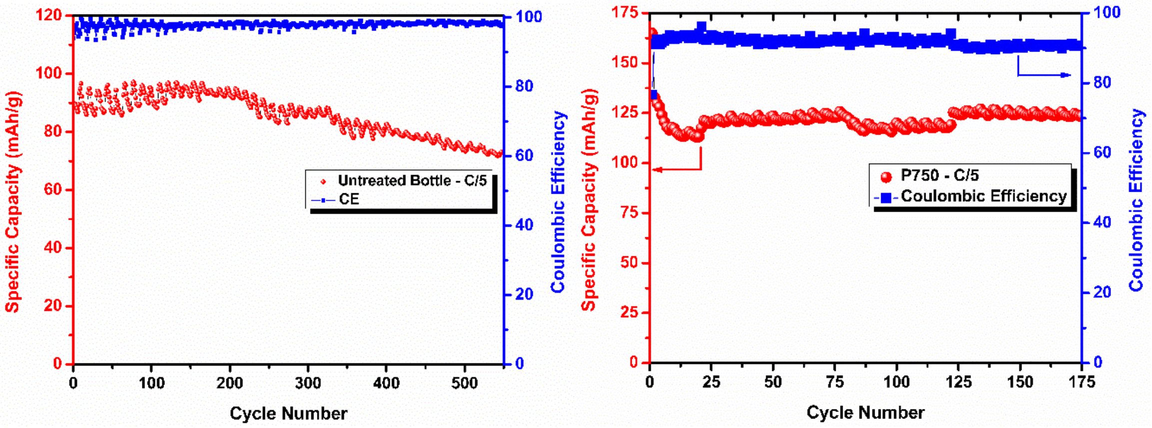

Figure. 2.13 Cycling data at the rate of C/5 for (a) untreated PET bottle, and (b) P750 (electrospun).

A charge/discharge rate of C/5 was employed to test the specific capacity of the PET-based devices. Figure 2.13a shows the C/5 charge/discharge cycling data of the unprocessed PET bottle, and figure 2.12b displays the C/5 cycling data of the electrospun sample. After completion of 548 cycles, the sample that was solely pyrolyzed fluctuated and had a specific capacity and Coulombic efficiency of 73 mAh/g and 97%, respectively. The capacity retention of the pyrolyzed bottle is equal to 81% of the initial value, 89 mAh/g. The average C/5 specific capacity for this cell was equal to 85.73 mAh/g. The electrospun sample showed more stability and had an average capacity of 175.88 mAh/g, a 205% increase in specific capacity (Fig. 2.13b). The significant capacity increase is ascribed to the higher surface area of the electrospun sample, where the higher surface area and structural voids can accommodate larger amounts of Li-ions.

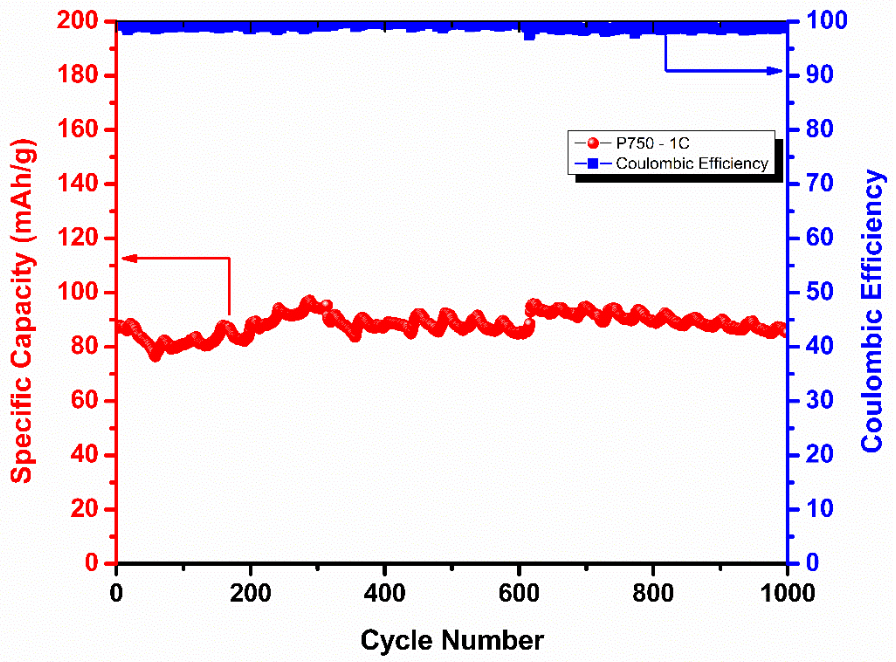

Figure 2.14. Longevity cycling test of P750 was conducted at 1C for 1000 cycles.

To test the material longevity, prolonged cycling was performed at the rate of 1C for 1000 cycles (approximately 8 years of normal use). From the data presented in figure 2.14, the material shows excellent stability with 98.06% capacity retention and Coulombic efficiency of 99.13% after the completion of 1000 cycles. This great stability makes P750 a good candidate for applications such as grid energy, solar cells, windmills, etc. To tune the specific capacity and make the material better suited for the more high-end applications, we introduced silicon nanoparticles in low concentrations and investigated the composition and electrochemical performance of the obtained material. The approach and results are presented in the next chapter.

2.4 Highlights

In this chapter, we introduced a scalable and industry mature preparation method to upcycle PET plastic waste to an activated carbon material for energy storage. By dissolving the PET plastic in a solvent mixture and using an electrospinning technique, PET nanofibers were formed. By controlled carbonization of the fibers, a microporous carbon network was produced, and its capability for energy storage was investigated. The analytical characterizations including Raman, SEM, EDS, XRD, BET, and TEM revealed the content of the material as aC and rGO. The electrochemical surveys consisting of CV, GCPL, and EIS showed that P750 performed as a EDLC with added pseudocapacitance. In addition, the employment of the developed PET-derived carbon as an anode active material in a LIB system was investigated. From the data, P750 displayed better electrochemical performance compared to P1100. The addition of carbon black and post-processing techniques were evaluated. The cycling data of P750 showed the merits of electrospinning where, in comparison to carbonized PET bottle (the starting material), a 206% increase in specific capacity was achieved. The longevity test of P750 showed great stability of the material, making it a good candidate for long-term energy storage with only 2% capacity fade after 1000 cycles at 1C cycling rate. Further material optimization can be achieved via different physical and chemical methods to make it better suited for various electrochemical applications. A brief summary of proposed enhancement methods is provided in chapter 5 for the reader.

Chapter 3

Silicon-Carbon Composite Anode Material Utilizing Upcycled PET Waste and Silicon Nanoparticles

In this chapter, we investigated the introduction and electrochemical performance of Si Nanoparticles (SiNPs) that were embedded in a carbon supporting frame generated from recycled PET waste. Seeing the performance of the PET upcycled carbon material, we introduced SiNPs to boost the performance and increase the specific capacity of the medium. In general, organic materials such as plastics can serve as a great source for activated carbon manufacturing because of their desired properties including, high surface area, porous network, good electronic conductivity, thermal and chemical stability.[93,94] Among plastics, PET is being used on a massive scale in different sectors of industry. There has been a growing number of research targeting the recovery of PET for energy storage applications. For example, milled PET particles that were recovered via a solvothermal process were employed as an anode medium in a LIB setup.[95] Półrolniczak et al. studied the synthesis of a hierarchical activated carbon that was generated from PET bottles and examined its application in a Li-S system.[96] In another study, with the aid of microwave radiation, an upcycled carbon material was obtained from PET waste. The energy sorting properties of the medium were studied and supported with DFT calculations.[97] Ko et al. presented the fabrication of synthetic graphene sheets and graphite from PET waste.[98] Also, PET waste was developed as an additive for an anode material with rate capability and capacity improvements.[99] In this work, SiNPs were homogeneously distributed in a PET solution via mechanical stirring and sonication. PET nanofibers encapsulating SiNPs (Si@PET) were produced via the electrospinning method. Afterwards, Si@PET went through carbonization to yield Si@C. Si@C was tested as an active anode material in a half-cell using Li metal for the counter electrode. The composition of the carbon frame, as well as the electrochemical performance of the developed anode material was investigated via, EIS, GITT, GCPL, and CV analyses. In short, a scalable and facile preparation method for developing a composite Si-C by the employment of commercial SiNPs and upcycled PET plastic is introduced.

3.1 Methods and Materials

3.1.1 Fiber production & Carbonization

We added commercial SiNPs (80 nm in diameter) to a homogenous 10 wt.% PET solution. The solution preparation method can be found in the previous chapter. The solvents were Trifluoroacetic Acid (TFA, Alfa Aesar, 99%) and Dichloromethane (DCM, Acros Organics, 99.9%, extra dry) with the ratio of 70 wt.% to 30 wt.%, respectively. We prepared several samples with different SiNP loading to find the optimum loading suitable for C-Si composite production. The samples that contained higher amounts of SiNPs (nominal loadings of 15.92, 12.62, and 11.22 wt.%) showed rapid capacity fading with poor specific capacity and cycling capability. In this regard, cell assembly was performed using the sample containing 8.77 wt.% of Si. To ensure uniform distribution of SiNPs in the solution mixture, the solution was mechanically stirred for 24 hours, followed by sonication for 1 hour before the spraying. Si@PET was developed using electrospinning methods. The electrospinning (Inovenso NE300 machinery) was performed with the following parameters: feeding rate of 720 µL h^{-1}, humidity level ~40%, spinneret at 12 cm from the collector plate, provided voltage ~19 kV. The carbonization (quartz tube furnace, MTI, OTF – 1200 X) was controlled in 2 steps at 760 Torr in a mixture of Ar and H_2 gas with the gas feeding rate of 50 and 200 SCCM for Hydrogen and argon, respectively. First, to preserve the fibers' conformation, the temperature was slowly ramped to 220 °C (5 °C min^{-1}) and was held at this temperature for 2 hours. Next, with the same heating rate, the temperature reached 750 °C and stayed at this set point for another 2 hours. After the sample was cooled down naturally, it was ball-milled (MTI, MSK -SFM-1 machinery) for further use. The as-prepared material was named Si@C.

3.1.2 Materials Characterization

SEM, EDS, XRD, and BET specifications are explained in section 2.1.2. The exact Si loading was investigated by Thermogravimetric Analysis based on the stoichiometric ratio of SiO_2 (TGA, Mettler Toledo machinery). TGA was performed from 25-850 °C with a heating rate of 30 °C min^{-1} using dry air (ultra-zero grade, Airgas) at the rate of 50 mL min^{-1}. To make sure of complete silicon oxidation, TGA was finished with a 3-hour isothermal step at 850 °C.

3.1.3 Cell Assembly & Electrochemical Characterization

We mixed Si@C with Polyacrylic Acid (PAA, the binder) and carbon black (the conductive agent) with a ratio of 80:10:10 wt.%, respectively. Carboxymethyl cellulose (CMC or cellulose gum) is another binder that is suitable for Si anode preparation. After the NMP solvent was added to the mixture, it was mechanically stirred for 24 hours to reach the appropriate uniformity and viscosity desired for casting. Next, by using a doctor blade, the slurry was cast on a copper foil and dried at 100 °C overnight. We calendared the casted slurry to the thickness of ~0.2 mm before punching and assembly in a coin-type cell (CR2032, MTI). The electrolyte solution was 1.0 M Lithium Hexafluorophosphate ($LiPF_6$) in a mixture of Ethylene Carbonate (EC) and Dimethyl Carbonate (DMC) solvents with a ratio of 1:1 (v/v). Pure Li metal chip served as the counter electrode. The simplified processing map along with the half-cell components are illustrated in figure 3.1.

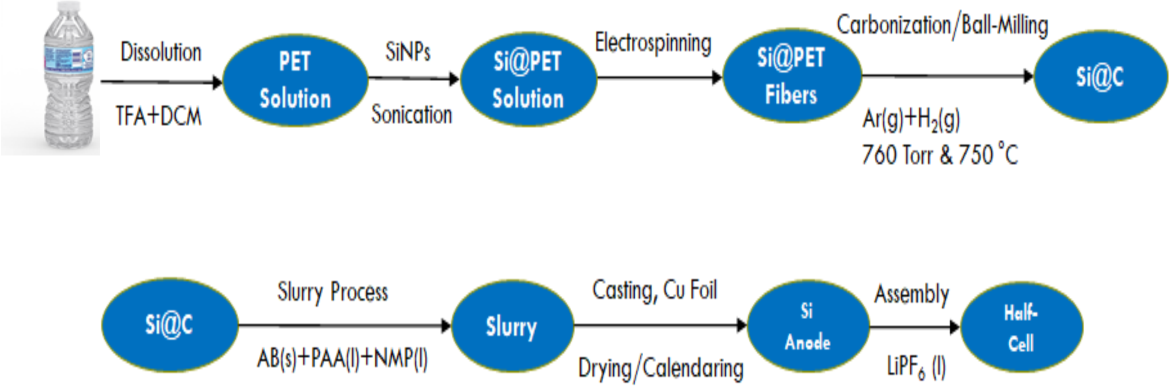

Fig. 3.1. Processing map of upcycling PET waste to Si-C composite anode material.

Cell assembly was performed in an argon-filled glovebox with water and oxygen levels below 1 ppm. All the electrochemical measurements were carried out on Bio-Logic testers (BCS 810 and VMP3 Potentiostat testing modules). CV was performed from 0-2 V at the scan rate of 0.1 mV s^{-1}. The potential window of 0-1 V was chosen for GCPL measurements under CC cycling. We conditioned the cell at C/50 (CC of 71.44 mA g^{-1}) for 4 cycles before cycling at C/10 (CC of 357.2 mA g^{-1}). The cycling currents were calculated based on the theoretical specific capacity of silicon (3572 mAh g^{-1} at room temperature). EIS characterization was carried out in the range of 10 mHz to 10 kHz at every 10 cycles with a 10 mV A.C. perturbation signal at fully charged and fully discharged states to eliminate the potential influence of the electrodes on another. GITT analysis was done with the applied current of 357.2 mA g^{-1} and a 10-minute rest interval from 0.01-1 V at every 40 cycles.

3.1.4 Computational Methods

To survey the structural interactions and binding properties of PET and SiNPs, we used the DFTB+ code [100] with the pbc/pbc-0-3[101–103] and ob2/ob2-1-1/base[104] sets of Slater Koster parameters. The primary structures of the studied silicon nanoparticles from 0.7 nm to 1.6 nm are shown in figure 3.3. SiNPs were collected from a bulk supercell from the diamond crystal structure. Only those atoms that fell under the desired radius were selected, and the rest were removed.

3.2 Results and Discussion

3.2.1 Analytical & Computational Characterization

The formation and composition of Si@PET and Si@C were investigated via SEM, Raman, XRD, and computational analyses. We observed that SiNPs were homogeneously distributed among the fibers, while the fibers were smooth, uniform, and very thin (Fig. 3.2). From Table 3.1, the mean value of fibers' diameter is equal to 0.76 μm while the range was 0.47-1.01 μm. To understand the relationship between silicon nanoparticles and PET, we used theoretical DFTB+ calculations. The size range of 71 atoms (0.7 nm) to 849 atoms (1.6 nm) was selected. Different primary adsorption configurations were tested, and the most optimized and stable configurations were adopted to explore the bindings of silicon nanoparticles and PET. Table 3.2 lists the binding energy of each studied case.

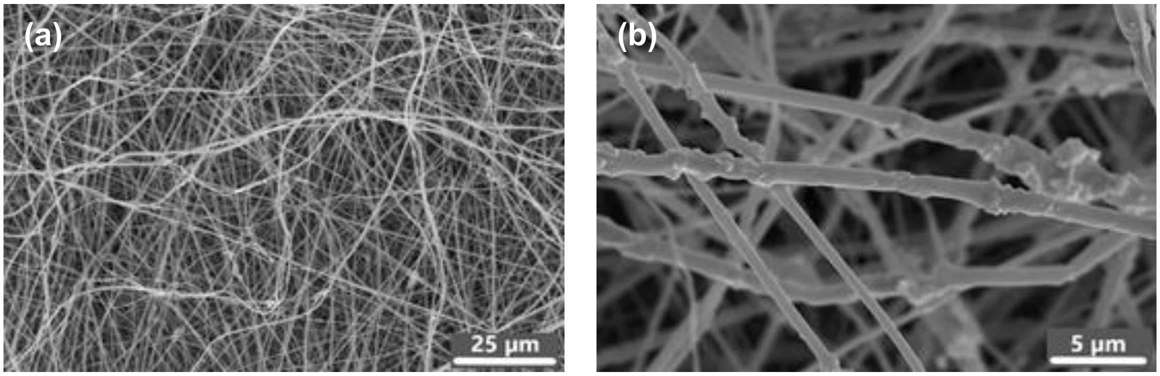

Figure 3.2. SEM images of Si@PET magnified to (a) 1,000x and (b) 5,000x. The development of a compressed forest of PET fibers enclosing Si particles, including some bulk Si clusters, is observed. From the figures, SINPs are traced along the fibers, providing a good distribution of NPs within the fibers network.

d1	**d2**	**d3**	**d4**	**d5**	**d6**	**d7**	**d8**	**d9**	**d10**	**d11**
0.478	0.502	0.529	0.579	0.59	0.599	0.611	0.656	0.691	0.711	0.771
d12	**d13**	**d14**	**d15**	**d16**	**d17**	**d18**	**d19**	**d20**	**d21**	**d22**
0.796	0.81	0.833	0.881	0.89	0.9	0.911	0.976	0.978	0.998	1.011
Min	**Max**	**Mean**	**St. D.**							
0.478	1.011	0.759	0.172							

Table 3.1. Mean, standard deviation, min and max values of the fiber diameters in µm.

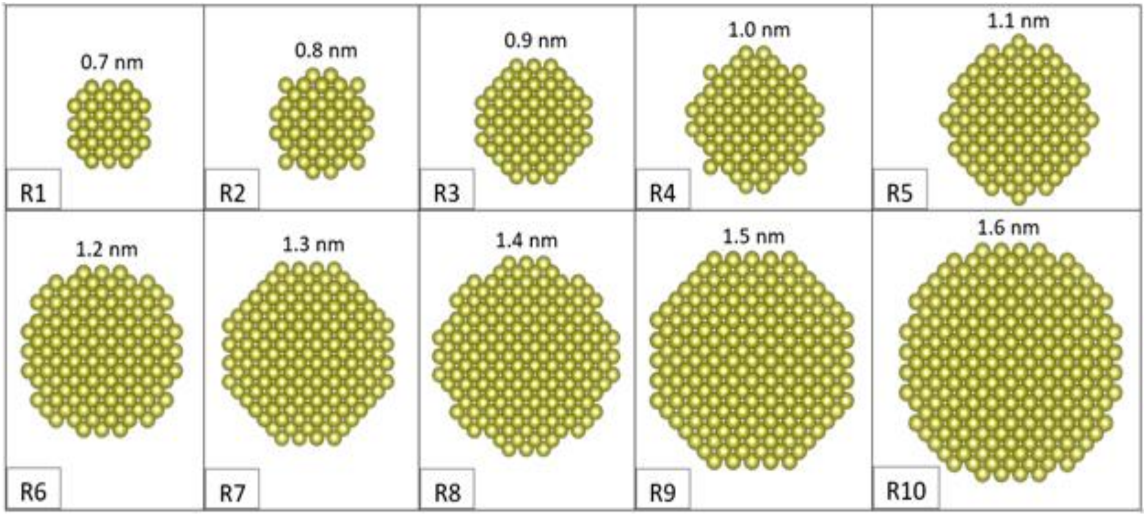

Figure 3.3. The optimized, initial structures and geometries of studied silicon nanoparticles from 0.7 to 1.6 nm.

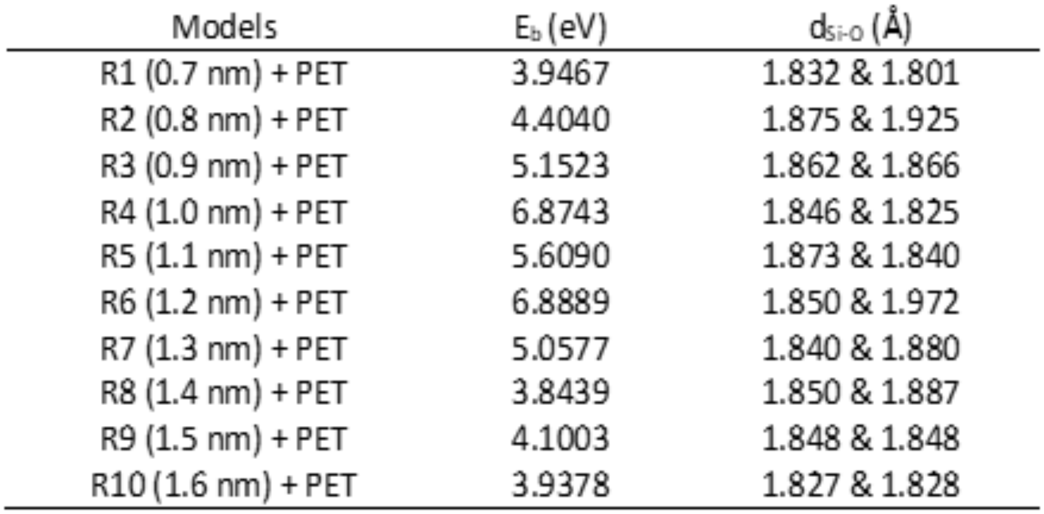

Models	E_b (eV)	$d_{Si\text{-}O}$ (Å)
R1 (0.7 nm) + PET	3.9467	1.832 & 1.801
R2 (0.8 nm) + PET	4.4040	1.875 & 1.925
R3 (0.9 nm) + PET	5.1523	1.862 & 1.866
R4 (1.0 nm) + PET	6.8743	1.846 & 1.825
R5 (1.1 nm) + PET	5.6090	1.873 & 1.840
R6 (1.2 nm) + PET	6.8889	1.850 & 1.972
R7 (1.3 nm) + PET	5.0577	1.840 & 1.880
R8 (1.4 nm) + PET	3.8439	1.850 & 1.887
R9 (1.5 nm) + PET	4.1003	1.848 & 1.848
R10 (1.6 nm) + PET	3.9378	1.827 & 1.828

Table 3.2. The binding energies (E_b) for each model and corresponding bond lengths ($d_{Si\text{-}O}$).

Figure 3.4 displays the optimized geometry of interactions between PET and silicon nanoparticles. From the image, the calculated binding energy of 6.89 eV for R=1.2 nm shows that PET binds very strongly to the NP-R6 surface for the PET+SiNP models. This indicates that the attraction is strongest for R6 (1.2nm followed by R4(1.0 nm)). Our analysis revealed that the most steady configuration is the result of the bindings between 2 silicon and 2 oxygen atoms. The bond angle was 122°, and the bond lengths were equal to 1.972 and 1.850 Å with respect to each O atom (Fig. 3.4)

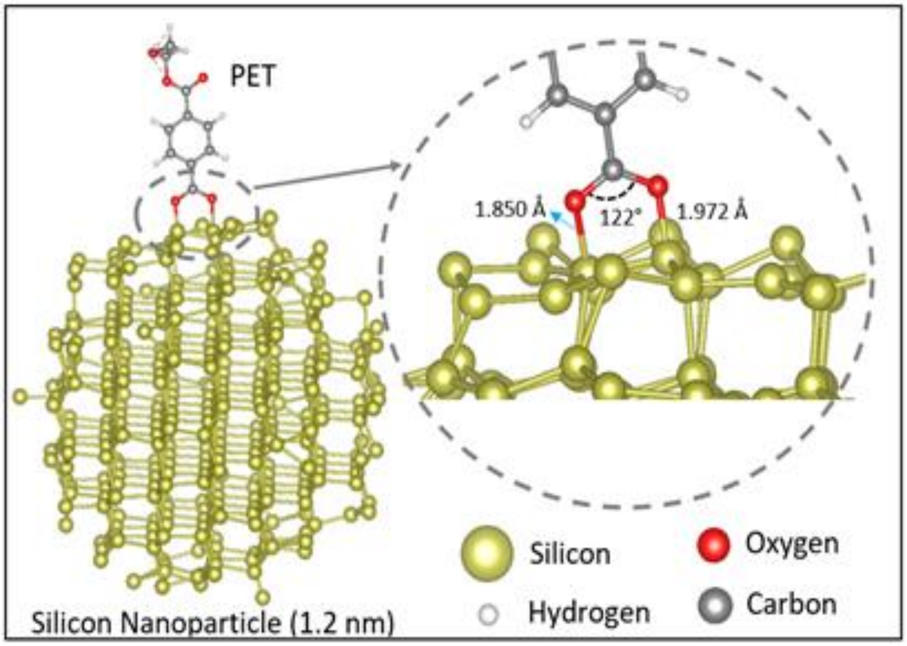

Figure 3.4. The optimized geometry of interactions between PET and SiNPs (1.2 nm). The most stable structure was observed when 2 O atoms of PET interacted with 2 Si atoms at an angle of 122°. The bond length variation was found to be very similar for all the tested conformations.

The semi-homogeneous distribution of SiNPs in the observed SEM images was assigned to the verified interactions of PET and SiNPs, which resulted in encapsulated SiNPs by PET. This can further assist with the electronic conductivity of Si that requires adjacent carbon atoms.

Raman spectroscopy assisted with defect density and graphitization degree study of the material. The Raman profile of Si@PET shown in figure 3.5, is a good match to the profile of untreated PET with the addition of Si, and silicon oxide peaks. The peaks at 518 cm^{-1}, and 960 cm^{-1} are related to the first and 2nd-order scattering of SiNPs, respectively. The peak at 1069 cm^{-1} is assigned to the vibrations of partially oxidized Si, Si-O.[105,106] The data can support the idea of the non-destructive dissolution process of PET which coincides with SiNPs insertion within the polymer structure. The Raman scan of Si@C included Carbon, Si, and silicon oxide peaks. From the image, the peaks at 304 cm^{-1} and 434 cm^{-1} are corresponding to Si-XII and Si-III phases, respectively, and they are related to the 2nd-order acoustic phonon mode of bulk silicon.[107]

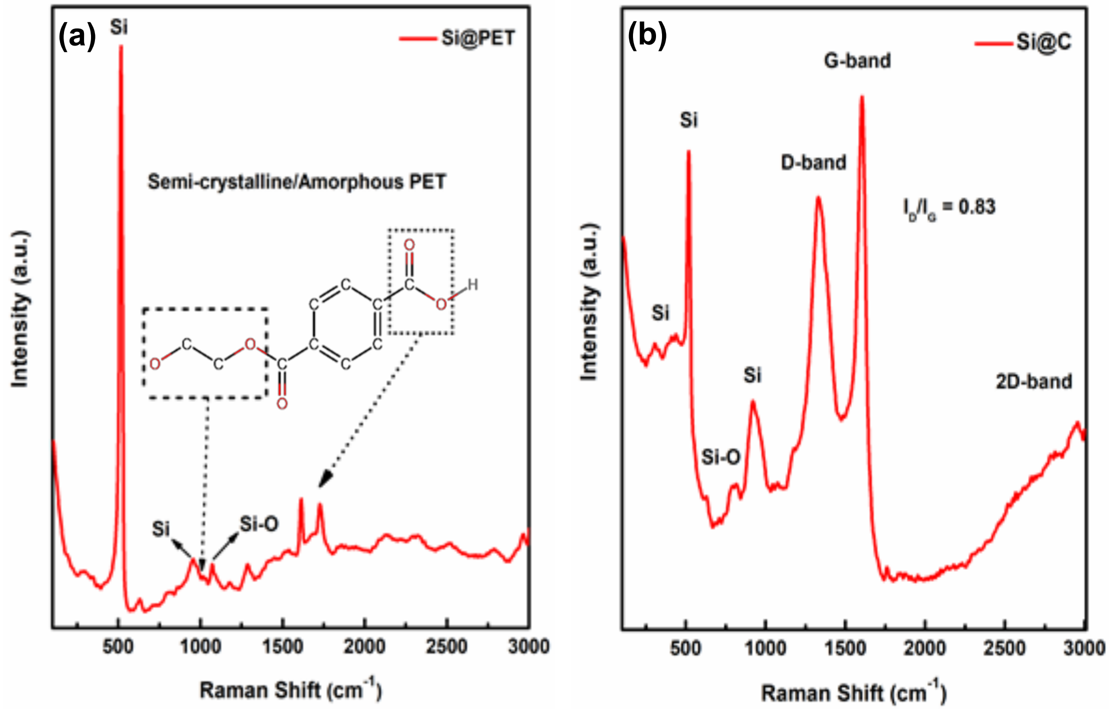

Figure 3.5. Raman spectra of the (a) electrospun PET fibers enclosing Si nanoparticles, indicating the presence of semi-crystalline/amorphous PET along with Si and silicon oxide peaks; and (b) milled carbonized sample, exhibiting the characteristics of Si, silicon oxide, amorphous carbon, and rGO. Silicon oxide peaks are related to the formation of partially oxidized SiNPs upon contact with air and during the carbonization steps.

Other Si peaks are observed at 520 and 929 cm^{-1}, corresponding to the first and 2nd-order scattering of crystalline Si, respectively.[108,109] Intrinsic vibrational modes of silica gave rise to the shoulder peak at 802 cm^{-1}.[110,111] Carbon peaks were observed at 1339 cm^{-1}(D-band), 1601 cm^{-1}(G-band), ~2500-3000 cm^{-1} with local peaks at 2842 and 2961 cm^{-1} (2D-Band). A detailed explanation of each peak is provided in the previous chapter for the reader. In summary, the presence of the aforementioned peaks is evidence for the existence of amorphous carbon and multi-layer rGO.[76–78,112]

The XRD profiles of Si@PET and Si@C are shown in figure 3.6. From image 3.6a, the peaks at 16.56° and 17.72° are characterized by (011) and (010) planes of PET, respectively.[113] Our study concluded that fibers are semi-crystalline/amorphous while the amorphous region is predominant.[114,115] The peaks at 28.37°, 47.74°, and 56.28° are related to silicon nanoparticles.[116]

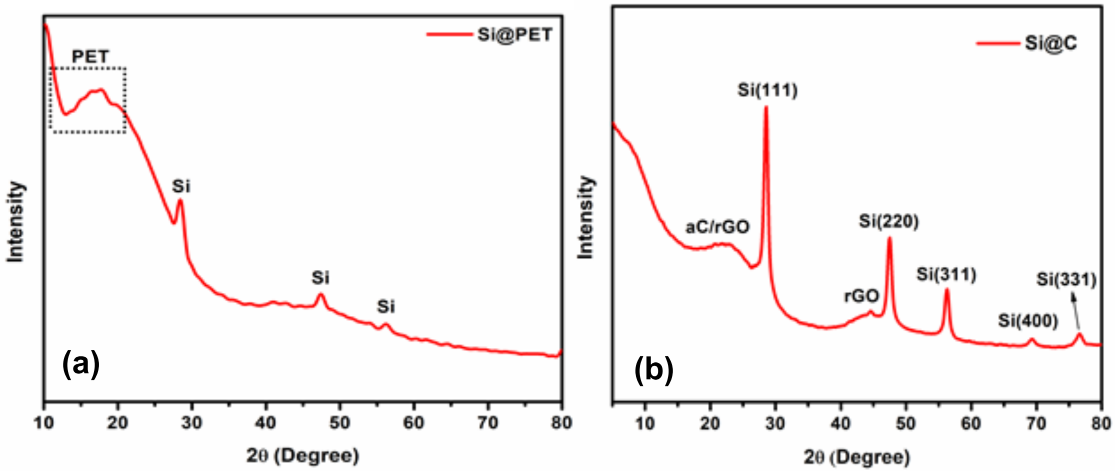

Figure 3.6. XRD profiles of (a) electrospun fibers, confirming the existence of mixed semi-crystalline and amorphous structure of PET along with Si characteristic peaks. The relatively low intensity of silicon peaks can be due to the coverage with PET fibers; and (b) milled carbonized sample, showing the presence of amorphous carbon (aC), rGO, and silicon.

The XRD scan of Si@C consists of carbon peaks at 21.73° and 44.58° with respective d-spacings of 4.08 and 2.03 Å, respectively (Fig. 3.6). These peaks are linked to aC and rGO.[80–82] The d-spacing of 4.08 Å in addition to the peak location implies that graphene oxide sheets are sufficiently reduced. The mixed-phase of the carbon frame is rooted in carbonized PET with a similar mixed structure. Crystalline silicon peaks were detected at 28.54°, 47.48°, 56.31°, 69.38°, and 76.56°, and further, they can be referred to the cubic phases of silicon.[116,117]

The BET survey of the material is presented in figure 3.7. BET analysis revealed a microporous structure with the surface area and pore size of 400.1 m^2 g^{-1} and 4.65 Å, respectively.

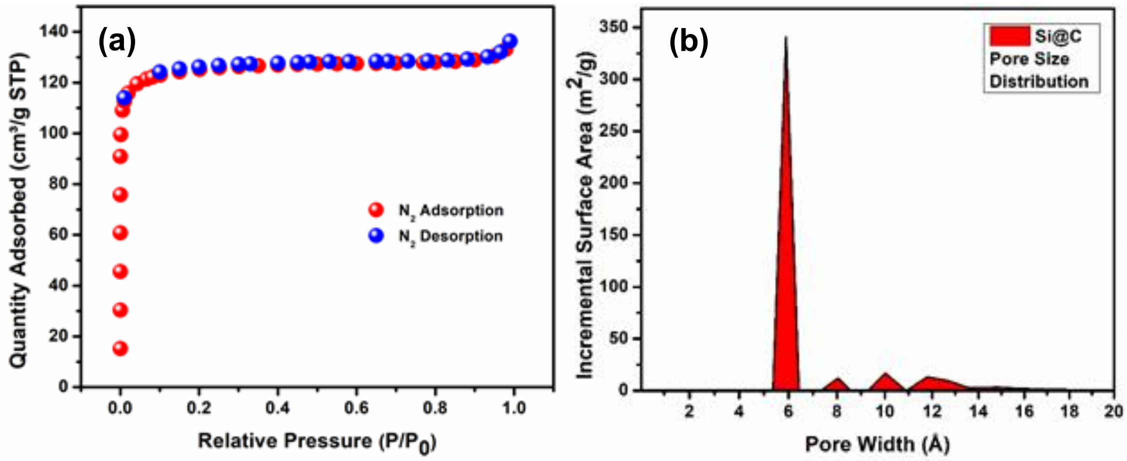

Figure 3.7. (a) N_2 adsorption/desorption isotherms of Si@C, identifying a microporous carbon structure with the surface area of 400.1 m^2 g^{-1}; and (b) relative pore volume distribution of the carbon network showing a relatively uniform porous structure with its pore size concentrating at 5.90 Å.

When we compared the BET data to that of P750, we found a great match of details between the two compounds. This finding implies that the carbon surface is not influenced by the NP addition, while the close distribution of the pore size speaks for uniform carbonized fibers.

TGA analysis (Fig. 3.8) was performed to calculate the exact mass of Si in the Si@C sample. The silicon loading was equal to 8.77% for our Si@C sample and 0.51 mg cm^{-2} for our tested device. The Si@C composite was assumed to be fully oxidized to SiO_2 upon removal of the carbon content in dry air at 850 °C.

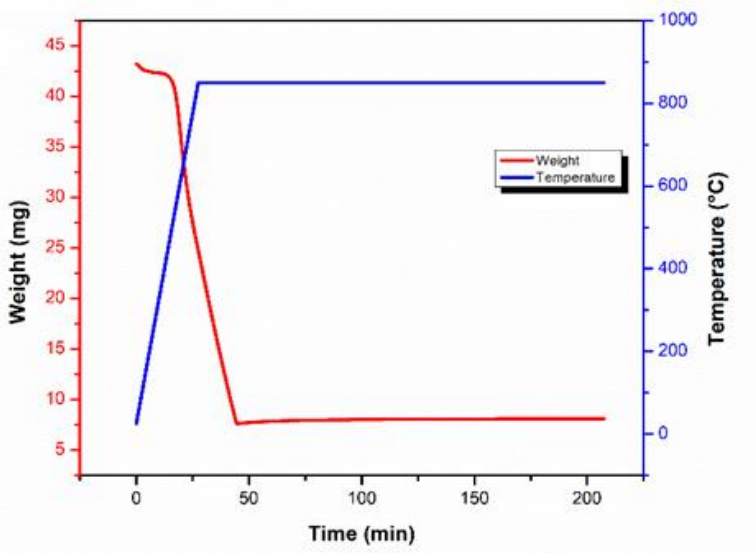

Figure 3.8. TGA profile of Si@C in dry air.

For the calculations, if we take x as the mass of Si and y for the mass of C in the Si@C sample out of 100 (corresponding to 100 wt.% at the beginning of TGA), then x+y=100. Initial weight of Si@C was equal to 43.194 mg which was decreased to 8.124 mg after TGA completion. At this point, all the carbon content was assumed to be removed and

SiNPs were fully oxidized to SiO_2. Therefore, $(60/28)x=18.80$ where, 28 represents the atomic weight of Si and 60 is assigned to the molecular mass of SiO_2. Therefore, it was calculated that $x=8.77$.

The SEM and EDS mapping of Si@C are shown in figure 3.9. The EDS data is in excellent agreement with our previous analysis indicating contributions from Carbon, silicon and oxygen. Silica and rGO are adding to the oxygen content.

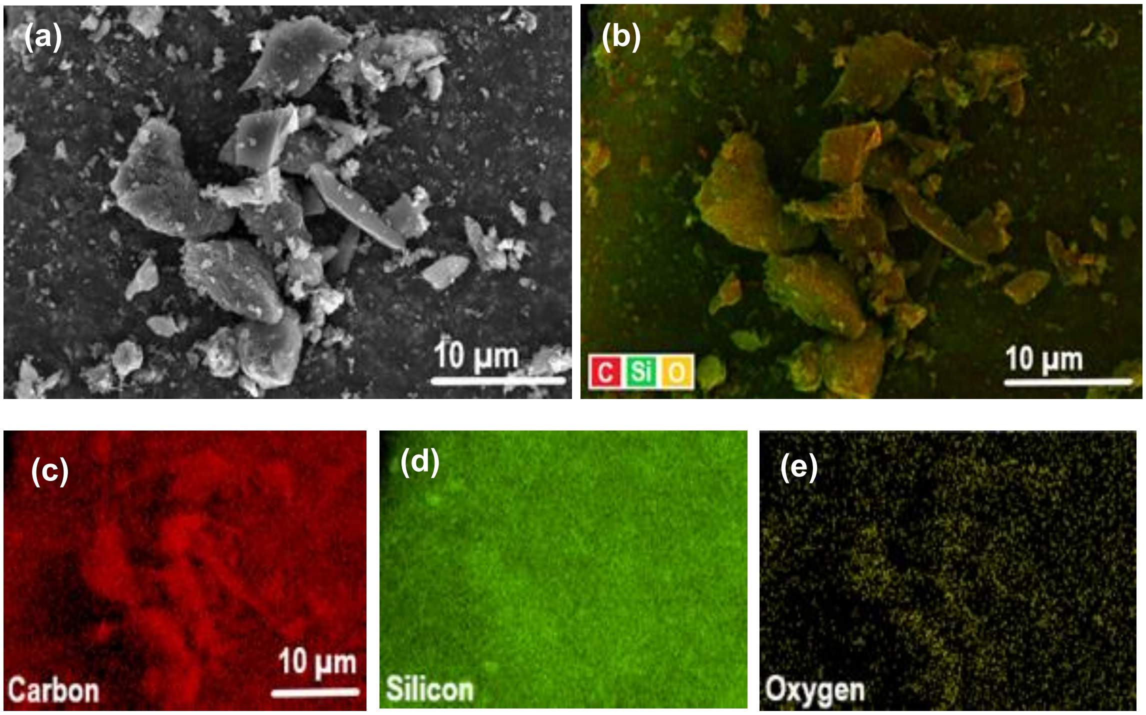

Figure 3.9. (a) SEM image of Si@C magnified to 3,500x, (b) EDS mapping of Si@C confirming the presence of C, Si, and O. EDS mapping of (c) Carbon, (d) Silicon, and (e) Oxygen elements. From the images, ample and uniform distribution of Si loading was noticed.

3.2.2 Electrochemical Measurements

Figure 3.10a shows the CV plots of Si@C at different cycles. The data is consistent with the typical redox behavior of Si with lithiation below 0.3 V and delithiation at 0.40 and 0.55 V.[118–122] The observed peak intensity increase with further cycling is related to the progressive activation of the material that can alloy with Li.[123] The anodic peaks at 0.40 V and 0.55 V are corresponding to the decomposition of $Li_{4.2}Si$, and further, they are related to amorphous Si.[121] The first broad cathodic peak from 0.1-0.7 V is related to the irreversible reactions of electrolyte and electrode resulting in SEI layer formation.[124,125] Such a broad peak was not detected with continued cycling. The peaks at 0.16 V are analogous to the dealloying phase of Li_XSi.[120,126] A similar curve shape was achieved after the 7th cycle, which can be related to a stable Li intercalation and extraction during the cycling. The voltage profile of the anode is consistent with our CV analysis. Comparing the CV profile of P750 (Fig. 2.12) to that of the C-Si composite, the capacity contribution is mainly related to SiNPs in the studied voltage range. However, the electrochemical calculations were based on the total mass of the electrode consisting of carbon and Si.

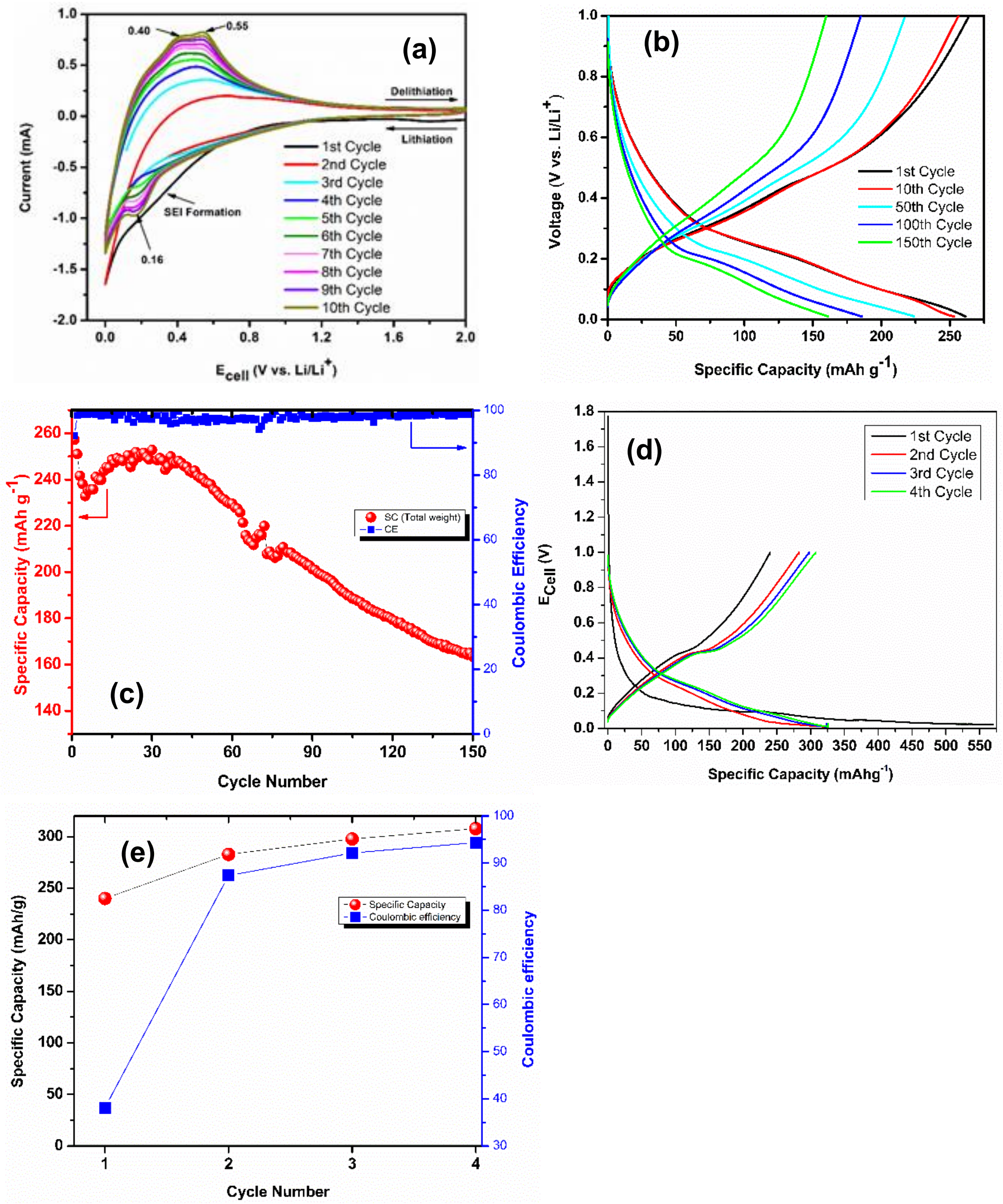

Figure 3.10. (a) cyclic voltammetry at a scan rate of 0.1 mVs^{-1}, exhibiting: characteristic properties of amorphous Si, and the presence of an activation process; (b) the charge/discharge voltage profiles of Si anode cycled at C/10. The results are in good agreement with our CV survey of Si@C; (c) the cycling performance and Coulombic efficiency of the Si anode; the device could retain 62% of its initial capacity after 150 cycles; (d) The voltage profile, and (e) Specific capacity and coulombic efficiency plots of the conditioning cycles at the rate of C/50.

To activate the majority of the material and construct a systematic SEI, the cells went through 4 conditioning (formation) cycles at C/50. From figure 3.10d, the long and flat plateau during the first charge cycle is consistent with crystalline Si behavior, and it is related to the reaction of crystalline SiNPs with Li to form Li_xSi. The subsequent charge/discharge curves are consistent with amorphous Si profiles. The corresponding initial specific capacity and CE were equal to 239.94 mAh g^{-1} and 38%, respectively. Upon the end of the 4th cycle, the SC and CE were promoted to 307.66 mAh g^{-1} and 94%, respectively. Low initial SC and CE are attributed to irreversible SEI construction.[35,127] The incremental capacity increase coinciding with CE improvement is related to the activation process and SEI layer formation. This continuous activation is linked to additional penetration of the electrolyte into the porous structure of the electrode.[128] The GCPL data of the cell cycling at C/10 is shown in figure 3.10c. We observed a gradual increase in capacity up to cycle 20. The studied cell discharged the reversible capacity of 250.49 mAh g^{-1} and 163.45 mAh g^{-1} after 20 and 150 cycles, respectively. The CE was at 98.59% after 150 cycles at C/10. Knowing the fast capacity decay of SiNPs associated with the high reactive nature of NPs, the detected performance of the cell can be assigned to one or more of the following: i) atoms carbon in the vicinity of SiNPs can help with poor electronic conductivity of silicon particles; ii) according to our BET data, the pore size of the carbon frame is concentrated around 5.9 Å. This semi-homogeneity can provide a steady Li-ion diffusion which can help with better utilization of the active material and reducing Li plating; iii) the amorphous structure of the carbon network with lots of voids and defects can function as a buffer layer and allow for some non-destructive volume expansion/contraction that can maintain the SEI.

The new advancements in increasing the cell energy density must be accompanied by failure and degradation mechanism studies to ensure a reliable cell and estimate the battery's state of health.[129] To understand the failure mechanism, EIS, GITT, and Differential Capacity analysis were carried out, and the data are summarized in figure 3.11. From figure 3.11a, the internal resistance of the cell increased rapidly with continuous cycling. The detected increase in the height of each pulse interval is notably larger for the charging cycles. In general, the increase in internal resistance is caused by an increase in electrolyte viscosity, concentration polarization, and deterioration of the electrode's structure. An increase in electrolyte resistance would increase the overall internal resistance during both charging and discharge processes. From the graph, such change might signal that as cycling goes deeper, it becomes harder for the ions to get out of the structure rather than migrating inside. The other dissimilarity is the left shift of the curves, which means that at the same charging/discharging rate, charging takes a longer time as the cycle number increases. Such a phenomenon is not normal for lithium silicon half cells since it means more lithium ions are moving out of the silicon-carbon anode than moving into it. To further investigate the active material, EIS Nyquist plots were collected. Since the final EIS results consist of the impedance from both electrodes, EIS was implemented at both fully charged and fully discharged states to minimize the influence of one electrode on another.

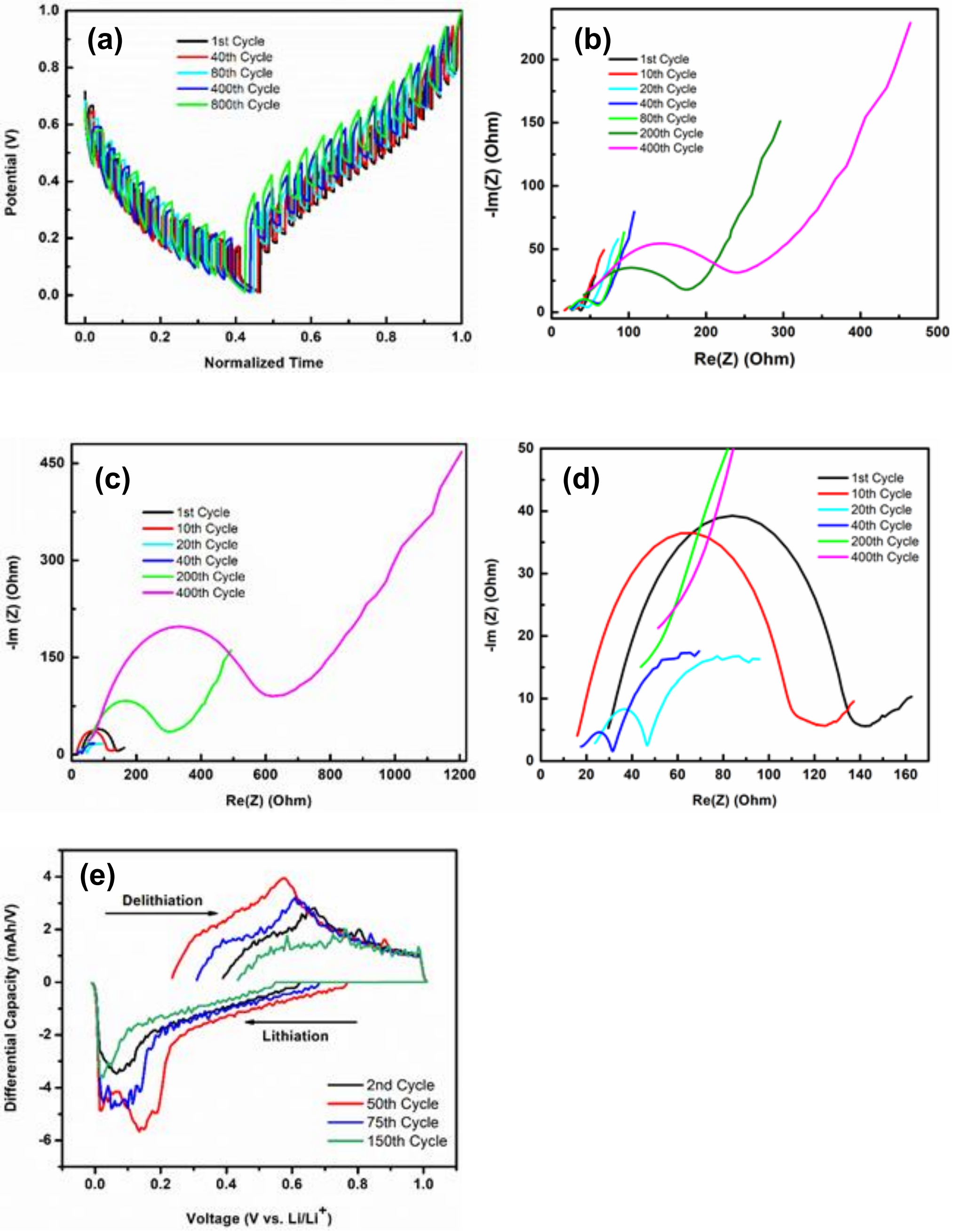

Figure 3.11. (a) GITT results at different cycles. The time axis is normalized to make sure of correct curve alignment. EIS Nyquist plot of cycles at (b) fully charged state (Li electrode), and (c) fully discharged state (Si@C electrode); (d) magnified Nyquist plot of discharged state from 0 to 200 Hz frequency range, the rapid change in the curvature of the diffusion tail is suggestive of a change in the structure of the active sites; (e) Differential Capacity plots at different cycles calculated from C/5 cycling data, confirming a shift in the supported active sites' structure.

Figure 3.11b shows the Nyquist plots at the fully charged state, which characterize the lithium anode. From the plot, we observed that while the plots keep almost the same shape, the scale of the semicircles grew larger with further cycling. This is due to the formation of a thin SEI layer as well as passivation of the lithium surface and formation of Li dendrites. Figure 3.11c shows the Nyquist plot of the fully discharged state that means that the silicon-carbon cathode is fully lithiated. In comparison to the Nyquist plots of the charged state: i) the magnitude of the peaks are increased much faster, and ii) at the low-frequency region, the curvature of the diffusion tail changes a lot at different cycle numbers (Fig. 3.11d). For the materials composed of different elements, the change of the diffusion tail is very significant because it can relate to the structural change of the electrodes, but it is often neglected by researchers. Zhu, et al. and Wang et al. showed that diffusion length and diffusion coefficient are the main parameters determining the curvature of the diffusion tail.[130,131] These parameters are in direct relationship to the thickness, pore size, and crystal structure of the active materials, and therefore, the curvature change can be indicative of a structural change. Such observation is very important since it means the fading of the capacity and the increase of the internal resistance may be related to a structural alteration. E. Casero et al. identified Reduced Graphene (RG) and Graphene Oxide (GO) by employing EIS and diffusion tail analysis. Since rGO is more ordered to GO, it would have a similar semicircle behavior in the ion discussion region (low frequency), but the magnitude of the semicircles would be smaller. Similar behavior was not observed for amorphous carbon and graphite. Since Si@C is composed of rGO and aC, the alloying probably started from the Si sites attached to rGO. Then, with continuous activation of the mainly amorphous structure of the carbon frame and the introduction of new active sites, the Li-ion diffusion route could change, and thus, the curvature of the diffusion tail was also changed. This consideration is in accordance with our GITT analysis that we summarized more Li-ions are moving out of the structure rather than migrating inside. This hypothesis can only be true if Li-ions are already in the structure in other forms. Table 3.3 summarized the curvature slope analyses of the material. From the table, it can be seen that the slope variation is higher for the fully discharged state for our device. From the table, while the slope variation of the fully charged state is much lower and maintains around 45° (corresponding to the typical semi-infinite behavior), the slope alteration is very high for the fully charged state due to the variation of the carbon network. The differential capacity vs. cell voltage profile that was obtained from cycling data is displayed in figure 3.11e. Analogous to CV, the peaks location and shape are corresponding to redox reactions at the electrodes. Since the anodic/cathodic curves are coupled to the lithiation/delithiation of amorphous Si, the loss of the peaks with continuous cycling can be assigned to a change in the Si active sites. This observation can further intensify our previous GITT and EIS explanations.

Cycle Number	**Fully Charged**	**Fully Discharged**
1	1.44527 (55.4 degrees)	0.24054 (13.5 degrees)
10	1.34962 (53.5 degrees)	0.27664 (15.5 degrees)
20	1.40743 (54.6 degrees)	0.86537 (40.9 degrees)
40	1.5996 (57.9 degrees)	0.97297 (44.2 degrees)
200	1.14175 (48.8 degrees)	0.66951 (33.8 degrees)
400	0.83701 (39.9 degrees)	0.66199 (33.8 degrees)

Table 3.3. Summary of slopes of diffusion tails at various cycle numbers.

The cell's diffusion coefficient at fully charged and fully discharged states were calculated using the equation 3.1:

$$D = \frac{4}{\pi \tau} \left(\frac{V_m n_m}{S}\right)^2 \left(\frac{\Delta Es}{\Delta Et}\right)^2 \qquad (3.1)$$

where, τ is the duration of the current pulse; Vm, and nm are the electrode's molar volume and the number of moles, respectively; and S is the electrode-electrolyte contact area. ΔE_s is the steady-state potential change and ΔE_t refers to the change in the overall cell voltage following the introduction of a current pulse in a single step GITT, excluding the IR drop. (Fig. 3.12)[133]

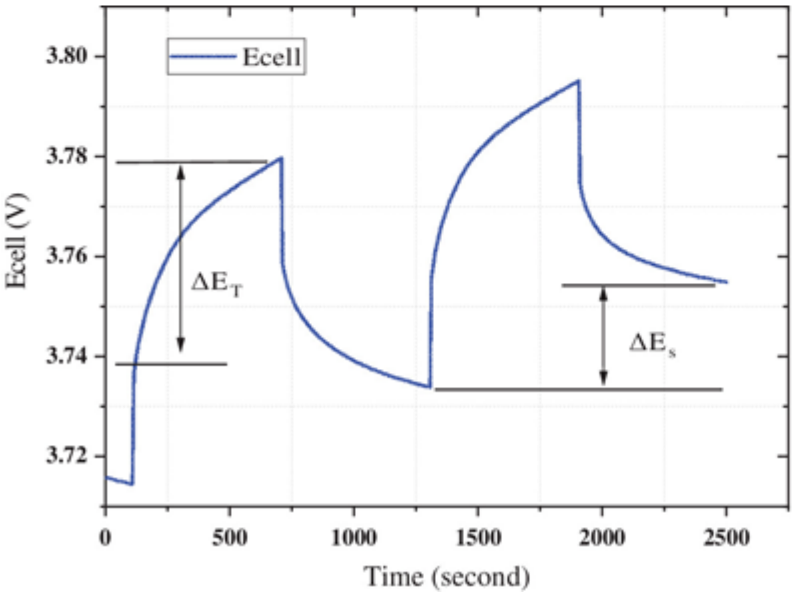

Figure 3.12. For the diffusion coefficient calculations, in a single GITT step, ΔE_s is the change in the steady-state voltage and ΔE_t relates to the overall cell voltage. The voltage change caused by the internal resistance is subtracted from the value.

To understand the diffusion coefficient variation, all the parameters except for the changes in potential were treated as constants. Therefore, the variance will depend on the ΔE_s and ΔE_t. Table 1 summarizes the calculated values along with the description of the observed changes.

Cycle Number	**Fully charged (~80%)**	**Fully discharged (0%)**	**Comments**
1st	**0.26548**	**0.17866**	Stimulation of the active material initiated.
40th	**0.42124**	**0.18598**	The increase of the diffusion behavior indicates the persistent activation of the material.
80th	**0.38254**	**0.10790**	The significant change of the diffusion coefficient is due to a change in the electrode's supported active sites (from mainly rGO to mostly aC).[132–134]
400th	**0.27873**	**0.11262**	The notable decrease of the diffusion coefficient at a fully charged state can be due to the growth of the passivation layers and dendrites on the anodic electrode. The small increase of the diffusion coefficient at a fully discharged state indicates the slow activation process of the aC due to its high surface area and relatively small pore size.
700th	**0.36949**	**0.10614**	The change in the diffusion coefficient is related to the decomposition and reformation of dendrites and the passivation layers on the anodic electrode along with a persistent passivation occurring on the cathodic side.

Table 3.4. Diffusion coefficient variation at different cycle numbers. The numbers do not represent actual values since they were calculated based on the detected voltage change for comparison purposes.

3.3 Highlights

In this chapter, a scalable method for producing composite Si-C anode active material for LIBs was introduced. SiNPs were used as Si precursors, and upcycled PET waste was employed as a conductive carbon frame. The electrospinning technique was used to develop PET films encapsulating SiNPs. To realize the synergistic effect between PET and SiNPs, DFTB+ calculations were performed, and the outcome revealed a close interaction between 2 oxygen atoms of PET and 2 Si atoms. This observation can assist with realizing the homogeneous distribution of NPs in the solution, fibers, and subsequently, the active material. We employed a series of analytical characterization including SEM, EDS, XRD, Raman, and BET analyses on the active material and understood that polycrystalline SiNPs were bordering with the carbon network consist of aC and rGO. Electrochemical characterizations including CV, GCPL, EIS, GITT, Differential Capacity, diffusion tail, and diffusion coefficient surveys identified the following: i) the carbon frame consists of aC and rGo, ii) Active sites alteration with prolonged cycling, iii) progressive activation of the material along with SEI layer formation during the conditioning cycles.

Chapter 4

Microporous Carbon Structure Generated from Upcycled PET Waste as a Host for Lithium-ion Battery Sulfur Cathode

This Chapter presents the strategy to employ the generated microporous carbon structure (P750) to host elemental sulfur as a cathode active material in a LIB setup. To obtain the C-S composite, powdered elemental sulfur was mechanically mixed with the carbon material and later was molten, and an interconnected network of sulfur and carbon was created.

4.1 Methods and Materials

Milled elemental sulfur (S, 99.99%) was mixed with P750 with the ratio of 1:1. The mixture was further ground to ensure good mixing. Then, the mixture was loaded in a quartz tube and was heated at 150 °C for 5 hours in a furnace. The hating rate was 5 °C

min^{-1}, and the carrier gas was Ar. We observed that higher processing temperatures than 150 °C will result in sulfur escape which will be deposited on the furnace tube, decreasing the sulfur loading. Afterwards, the sample was cooled down naturally and was collected for further use. A coin-type (CR2032) Li-S battery was prepared using the P750/S electrode as the cathode and lithium metal chip as the anode. The electrolyte was 1 M bis(trifluoromethane)sulfonimide (LiTSFI, Sigma-Aldrich) lithium salt in 1,2-dimethoxyethane (DME) and 1,3-dioxolane (DOL, 1:1 in volume) solvents with 0.5 M $LiNO_3$ additive. The battery was assembled in argon-filled glove box with an O_2 and H_2O content of less than 1 ppm.

4.2 Electrochemical Characterizations

The battery with P750/S electrode was galvanostatically discharged/charged between 1.7 – 2.8 V using a Bio-Logic (BCS 810 Testing Module) battery tester. The sulfur loading in the P750/S electrode was 0.6 mg cm^{-2}. The specific capacity values were calculated based on the sulfur active material weight. The cells were conditioned for 3 cycles before cycling at a higher current rate. The 3 conditioning cycles consisted of a two-step galvanostatic discharge: In the first step (from 2.8 V to 2.1 V) a current rate of C/50 (1 C = 1675 mAh/g) was used for the reduction of sulfur to long-chain lithium polysulfides; whereas in the second step (from 2.1 V to 1.7 V) C/100 was used to provide a longer time for the conversion from long-chain to short-chain polysulfides. This plateau-targeted conditioning of sulfur was adopted from the previous work from our group.[135] A galvanostatic current with a rate of C/50 was applied throughout the charging step in the conditioning cycles. After conditioning, the cells were discharged/charged at a relatively higher current rate of C/10. Figure 4.1a shows the cycling performance of the P750/S electrode. The battery demonstrates an initial capacity of 1464 mAh/g, which is 87% of the theoretical capacity of sulfur (1675 mAh/g), indicating a high active material utilization with a good wetting of the electrode by the electrolyte. The capacity decreases in the following conditioning cycles after the rearrangement of sulfur into more electrochemically favorable positions. The capacity decay is also likely due to polysulfide shuttling, in which the soluble polysulfides that are released from the cathode into the electrolyte migrate to the anode and passivate the anode surface by reduction and deposition.

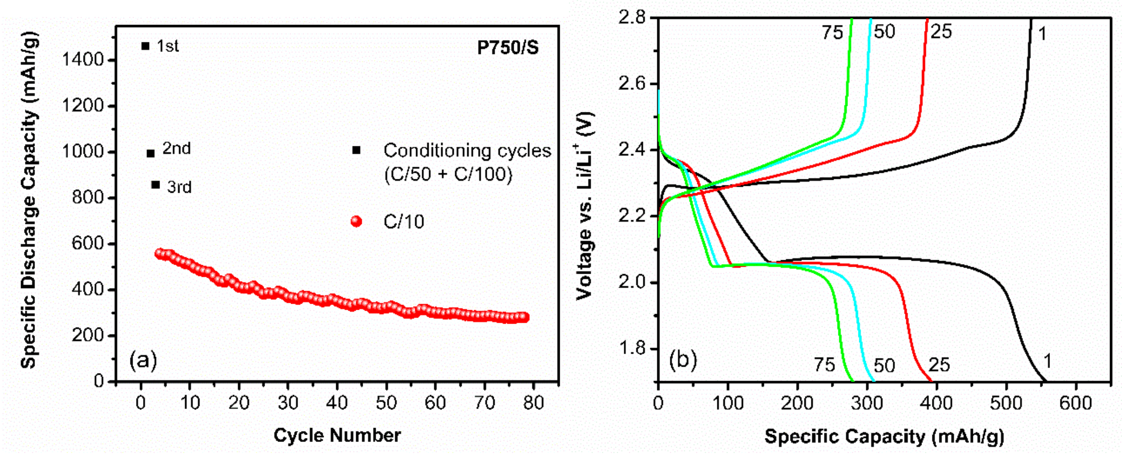

Figure 4.1. (a) Cycling performance of the Li-S cell prepared with P750/S electrode and (b) voltage profiles in the 1st, 25th, 50th and 75th cycles.

These processes may be responsible for the fast capacity decay since they could lead to the gradual loss of active material during cycling. When the current rate increases to C/10, a capacity of 558 mAh/g is delivered by the cell initially. Then the capacity decreases gradually with increasing cycle number, almost stabilizing at 280 mAh/g at the end of the 75th cycle at C/10. After 75 cycles, the cell prepared with P750/S electrode can still deliver a capacity that is 100 % greater than that of a commercial $LiCoO_2$ cathode (~140 mAh/g). Figure 4.1b displays the voltage profiles in the 1st, 25th, 50th, and 75th cycles. During discharge, profiles exhibit two voltage plateaus at ~2.4 V and ~2.1 V, associated with the reduction of elemental sulfur to soluble long-chain lithium polysulfides (Li_2S_n, $4 \leq n \leq 8$) and further reduction of long-chain polysulfides to insoluble short-chain polysulfides ($Li_2S_{(2)}$), respectively. Charge profiles also exhibit a two-stage reverse reaction with a long plateau at ~2.3 V and a shorter plateau at ~2.4 V, which are related to the oxidation of $Li_2S_{(2)}$ to long-chain polysulfides and further oxidation of long-chain polysulfides to elemental sulfur.[136,137]

Chapter 5

Recommendations for Future Research

This dissertation described the methodology to develop energy sorting mediums by recycling PET plastic waste and introducing active elements via simple yet effective and scalable methods. A microporous carbon structure that holds principal application in supercapacitors was prepared via fiberization and carbonization of PET. The plastic needs to be dissolved in a solvent suitable for fiber production. Table 5.1 is meant to be a shorthand list of what common solvents can be used to dissolve common plastics and is in no way limiting. The technique requires that you first dissolve a plastic before further processing in the manner (or similar manner) described before in the experimental details. Later, we introduced SiNPs and elemental sulfur to prepare anode and cathode active materials and tested their application in LIB setup. However, the materials' behavior can be further tailored via different chemical and physical treatments to make them better suited for more specific applications. Here, some of the recommendations for post-processing are provided for the reader. The electronic structure and surface chemistry of carbon-based material can be tuned via the introduction of dopants such as nitrogen[137,138], boron[139–141], and phosphorus[142,143]. As an example, Elessawy et al. reported on the fabrication of a 3D porous carbon structure doped with nitrogen atoms. For this purpose, they used urea and reduced PET at high temperatures.[144] The porosity and surface area of carbon materials can be modified by chemical etching using KOH and K_2CO_3. By carbon removal at high temperatures, new pores can be introduced as well as modifying the existing pores.[145] Material activation can be further promoted by implementing different exfoliation techniques because by removing the interlayer interactions and opening new active sites, ion diffusion can be enhanced further. The strategies include electrochemical intercalation[146], mechanical exfoliation[147,148], and chemical exfoliation[149]. For EDLCs, energy density improvements can be obtained via i) decorating the surface with nitrogen and oxygen functional groups[150], ii) equipment of electrolyte with redox-active materials[151], iii) selection of electrolyte with compatible ion size with respect to the material's pore size[152], iv) application of organic and ionic liquid electrolytes that can benefit with a wider temperature tolerance and cell voltage range[153]. The application of SiNPs for manufacturing Si electrodes brings challenges, including low Coulombic efficiency, potential side reactions due to the high surface area of NPs. In addition, Si has a low voltage, and it consumes Li to form the SEI layer that can result in poor cycle life. The relatively low density of Si nano-powders makes the volumetric energy density of the battery low, which is a critical parameter for applications in EVs and HEVs.

Plastic Type:	Dissolves or Decomposes in:
Acrylonitrile Butadiene Styrene (ABS)	Acetaldehyde, Acetone, Amyl Acetate, Benzene, Butyric Acid, Carbon Tetrachloride, Chloroform, Ehtyl Acetate, Ethylene Dichloride, Methyl Ethyl Ketone, Naphthalene, Silicone Fluids, Sulfur Dioxide, Toluene, Turpentine, Xylene
Acetal Plastic (POM)	Formic Acid, Hydrofluoric Acid, Hydrogen Peroxide, Nitric Acid, Phenol, Sulfuric Acid
Acrylics	Acetaldehyde, Acetone, Alcohols, Amyl Acetate, Anilline, Benzene, Butyric Acid, Chlororsulphonic Acid, Chromic Acid, Ethyl Acetate, Formic Acid, Methyl Ethyl Ketone, Sulfuric Acid, Xylene
Cellulose Acetate Butyrate (CAB)	Benzene, Chloroform, Cyclohexanone, Ethylene Glycol, Methyl Acetate, Methyl Ethyl Ketone, Methyl Chloride, Nitric Acid, Styrene, Toluene, Trichlorethylene, Xylene
Chlorinated Polyvinyl Chloride (CPVC)	Acetaldehyde, Acetone, Anillne, Benzene, Bromine, Chloroform, Cyclohexanol, Cyclohexanone, Ethylene Dichloride, Methyl Ethyl Ketone, Methyl Chloride, Naphthalene, Toluene, Tricholethylene, Xylene
High Density Polyethylene (HDPE)	Amyl Acetate, Benzene, Bromine, Butyric Acid, Carbon Tetrachloride, Chloral Hydrate, Chlororsulphonic Acid, Cresylic Acid, Cyclohexanol, Cyclohexanone, Ethylene Dichloride, Iodine in alcohol, Linseed Oil, Methyl Ethyl Ketone, Methyl Chloride, Ozone, Propane Gas, Toluene, Trichlorethylene, Turpentine, Xylene
Nylon, Type 6/6	Benzene Sulphonic Acid, Boron Trifluoride, Bromine, Calcium Hypochlorite, Chloral Hydrate, Chlorine, Chloroform, Chlorosulphonic Acid, Cresylic Acid, Fluorine, Fluosilicic Acid, Hydrobromic Acid, Hydrogen Peroxide, Iodine in alcohol, Nitric Acid, Perchloric Acid, Phenol, Phosphoric Acid, Sodium Hypochlorite, Sulphuric Acid, Sulphurous Acid, Xylene, Xylenol
Polyether Ether Ketone (PEEK)	Fluorine, Hydrobromic Acid, Phenol
Polyethylene Terephthalate (PET)	Chloroform, Methyl Chloride, TFA

Polycarbonate (PC)	Acetic Acid, Ammonium Carbonate, Benzene, Chloroform, Ethyl Acetate, Methyl Ethyl Ketone, Methyl Chloride, Ozone, Toluene, Turpentine
Polypropylene (PP)	Amyl Acetate, Benzene, Bromine, Butyric Acid, Carbon Tetrachloride, Chloral Hydrate, Chloroform, Cresylic Acid, Cyclohexanol, Cyclohexanone, Ethylene Dichloride, Methyl Ethyl Ketone, Methyl Chloride, Toluene, Trichlorethylene, Turpentine, Xylene
Polysulfones	Benzene, Chlorine, Chloroform, Chromic Acid, Cyclohexanone, Methyl Ethyl Ketone, Methyl Chloride, Toluene, Trichlorethylene, Xylene
Polyphenylene Sulfide (PPS)	Chlorosulphonic Acid, Hydrofluoric Acid,
Polyvinyl Chloride (PVC), Type I	Acetaldehyde, Acetone, Amyl Acetate, Aniline, Benzene, Chloroform, Cyclohexanol, Cyclohexanone, Ethyl Acetate, Ethylene Dichloride, Methyl Ethyl Ketone, Methyl Chloride, Naphthalene, Toluene, Trichlorethylene, Xylene
Polyvinyl Chloride (PVC), Type II	Acetaldehyde, Acetone, Amyl Acetate, Aniline, Benzene, Bromine, Butanol, Butyric Acid, Carbon Tetrachloride, Chloroform, Chromic Acid, Cyclohexanol, Cyclohexanone, Ethyl Acetate, Ethylene Dichloride, Methyl Ethyl Ketone, Methyl Chloride, Naphthalene, Toluene, Trichlorethylene, Xylene
Polyvinylidene (Di)Fluoride (PVDF)	Acetaldehyde, Acetone, Ammonia Gas, Chlorosulfonic Acid, Dibutylphthalate, Ethyl Acetate, Methyl Ethyl Ketone,

Table 5.1: List of common plastics and the solvents they are known to dissolve or decompose in. Chemical Resistance Chart https://www.plasticsintl.com/chemical-resistance-chart (accessed Feb 29, 2019).

Surface coating can mitigate side reactions. For practical application of such Si anode, the manufacturing cost of nano-sized Si structures needs to be reduced. For Li-S systems, infinite volume expansion of the Li anode and high electrolyte to the sulfur ratio of the battery are among the main challenges. An optimized electrolyte to sulfur ratio is needed to utilize all the accessible active sites, increase the cycle life, and reach for a higher energy density. Application of solid-state electrolytes can benefit LIB with the elimination of unwanted side reactions associated with liquid electrolytes. Considering the environmental hazards linked to different battery components, future active materials are required to be environmentally benign, abundant, and cost-effective. This dissertation investigated upcycling of PET waste for energy storage by introducing different active materials. A series of analytical and electrochemical characterization methods were used to explore the content, composition, structure, and performance of the active materials. I hope that better resolutions can be effective in designing energy storage devices that can promote a sustainable society and minimize the extreme consequences of fossil fuel consumption.

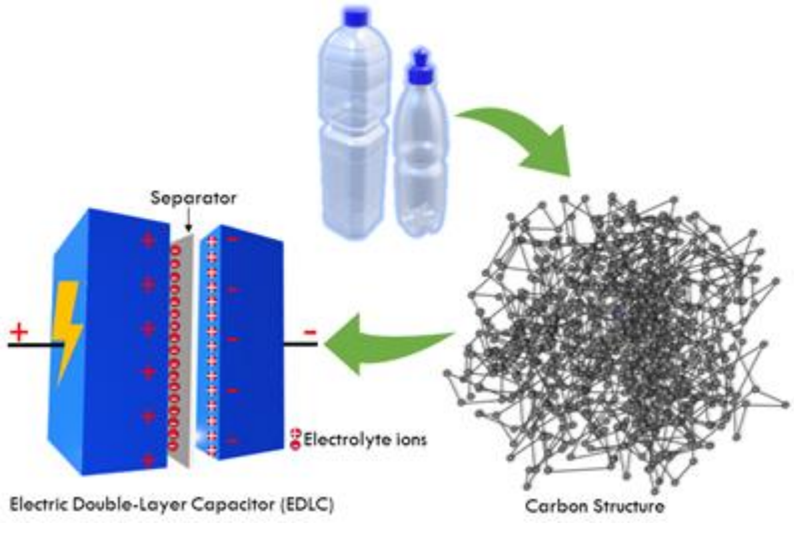

Figure 5.1. Plastic bottle waste with PET formula was upcycled to a carbon structure which was employed in the Electric Double-Layer Capacitor (EDLC).

Bibliography

1. Europe, P. Plastics-The Facts 2013: An analysis of European latest plastics production, demand and waste data. *Plastic Europe* 1–40 (2013).

2. Jambeck, J. R. *et al.* Plastic waste inputs from land into the ocean. *Science* **347**, 768–771 (2015).

3. National Research Council (U.S.). Study Panel on Assessing Potential Ocean Pollutants. *Assessing Potential Ocean Pollutants: A Report of the Study Panel on Assessing Potential Ocean Pollutants to the Ocean Affairs Board, Commission on Natural Resources, National Research Council*. (National Academies, 1975).

4. Appendix I: Summary of U.s. environmental protection agency data on solid-waste generation, disposal, and recycling in the United States. in *Recycling Reconsidered* (The MIT Press, 2011). doi:10.7551/mitpress/8829.003.0010.

5. Gasperi, J. *et al.* Microplastics in air: are we breathing it in? *Current Opinion in Environmental Science & Health* **1**, 1–5 (2018).

6. Eriksen, M. *et al.* Plastic Pollution in the World's Oceans: More than 5 Trillion Plastic Pieces Weighing over 250,000 Tons Afloat at Sea. *PLoS ONE* vol. 9 e111913 (2014).

7. Rochman, C. M., Kurobe, T., Flores, I. & Teh, S. J. Early warning signs of endocrine disruption in adult fish from the ingestion of polyethylene with and without sorbed chemical pollutants from the marine environment. *Sci. Total Environ.* **493**, 656–661 (2014).

8. Teuten, E. L., Rowland, S. J., Galloway, T. S. & Thompson, R. C. Potential for plastics to transport hydrophobic contaminants. *Environ. Sci. Technol.* **41**, 7759–7764 (2007).

9. Mato, Y. *et al.* Plastic resin pellets as a transport medium for toxic chemicals in the marine environment. *Environ. Sci. Technol.* **35**, 318–324 (2001).

10. Teuten, E. L. *et al.* Transport and release of chemicals from plastics to the environment and to wildlife. *Philos. Trans. R. Soc. Lond. B Biol. Sci.* **364**, 2027–2045 (2009).

11. Eriksen, M. *et al.* Plastic pollution in the South Pacific subtropical gyre. *Mar. Pollut. Bull.* **68**, 71–76 (2013).

12. Reisser, J. *et al.* Marine plastic pollution in waters around Australia: characteristics, concentrations, and pathways. *PLoS One* **8**, e80466 (2013).

13. Collignon, A. *et al.* Neustonic microplastic and zooplankton in the North Western Mediterranean Sea. *Mar. Pollut. Bull.* **64**, 861–864 (2012).

14. Rochman, C. M. *et al.* Policy: Classify plastic waste as hazardous. *Nature* **494**, 169–171 (2013).

15. Ji, L. N. Study on Preparation Process and Properties of Polyethylene Terephthalate (PET). *Applied Mechanics and Materials* vol. 312 406–410 (2013).

16. Choudhary, R., Kumar, A. & Murkute, K. Properties of Waste Polyethylene Terephthalate (PET) Modified Asphalt Mixes: Dependence on PET Size, PET Content, and Mixing Process. *Periodica Polytechnica Civil Engineering* (2018) doi:10.3311/ppci.10797.

17. Solomon, S., Plattner, G.-K., Knutti, R. & Friedlingstein, P. Irreversible climate change due to carbon dioxide emissions. *Proc. Natl. Acad. Sci. U. S. A.* **106**, 1704–1709 (2009).

18. Soylu, S. *Electric Vehicles: The Benefits and Barriers*. (BoD – Books on Demand, 2011).

19. Loehle, C. & LeBlanc, D. Model-based assessments of climate change effects on forests: a critical review. *Ecol. Modell.* **90**, 1–31 (1996).

20. Lal, R. Soil carbon sequestration impacts on global climate change and food security. *Science* **304**, 1623–1627 (2004).

21. Durance, I. & Ormerod, S. J. Climate change effects on upland stream macroinvertebrates over a 25-year period. *Glob. Chang. Biol.* **13**, 942–957 (2007).

22. Kumar, Y. *et al.* Wind energy: Trends and enabling technologies. *Renewable and Sustainable Energy Reviews* vol. 53 209–224 (2016).

23. Barnett, T. P., Adam, J. C. & Lettenmaier, D. P. Potential impacts of a warming climate on water availability in snow-dominated regions. *Nature* **438**, 303–309 (2005).

24. Kroeker, K. J., Kordas, R. L., Crim, R. N. & Singh, G. G. Meta-analysis reveals negative yet variable effects of ocean acidification on marine organisms. *Ecol. Lett.* **13**, 1419–1434 (2010).

25. Kurihara, H. Effects of CO2-driven ocean acidification on the early developmental stages of invertebrates. *Mar. Ecol. Prog. Ser.* **373**, 275–284 (2008).

26. Nerem, R. S. *et al.* Climate-change–driven accelerated sea-level rise detected in the altimeter era. *Proc. Natl. Acad. Sci. U. S. A.* **115**, 2022–2025 (2018).

27. *Climate change - realities, impacts over ice cap, sea level and risks*. (InTech, 2013). doi:10.5772/3459.

28. Westerling, A. L., Hidalgo, H. G., Cayan, D. R. & Swetnam, T. W. Warming and earlier spring increase western U.S. forest wildfire activity. *Science* **313**, 940–943 (2006).

29. Gleick, P. H. Water, Drought, Climate Change, and Conflict in Syria. *Weather, Climate, and Society* **6**, 331–340 (2014).

30. Diffenbaugh, N. S., Swain, D. L. & Touma, D. Anthropogenic warming has increased drought risk in California. *Proc. Natl. Acad. Sci. U. S. A.* **112**, 3931–3936 (2015).

31. Wu, H. & Cui, Y. Designing nanostructured Si anodes for high energy lithium ion batteries. *Nano Today* **7**, 414–429 (2012).

32. Liu, C., Neale, Z. G. & Cao, G. Understanding electrochemical potentials of cathode materials in rechargeable batteries. *Mater. Today* **19**, 109–123 (2016).

33. Wang, G., Shen, X., Yao, J. & Park, J. Graphene nanosheets for enhanced lithium storage in lithium ion batteries. *Carbon N. Y.* **47**, 2049–2053 (2009).

34. de las Casas, C. & Li, W. A review of application of carbon nanotubes for lithium ion battery anode material. *J. Power Sources* **208**, 74–85 (2012).

35. Qie, L. *et al.* Nitrogen-doped porous carbon nanofiber webs as anodes for lithium ion batteries with a superhigh capacity and rate capability. *Adv. Mater.* **24**, 2047–2050 (2012).

36. Wei, Q. *et al.* Novel bread-like nitrogen-doped carbon anchored nano-silicon as high-stable anode for lithium-ion batteries. *Appl. Surf. Sci.* **511**, 145609 (2020).

37. Zhang, X. *et al.* Facile fabrication of SiO2 nanotubes coated with nitrogen-doped carbon layers as high-performance anodes for lithium-ion batteries. *Ceram. Int.* **47**, 1373–1380 (2021).

38. Zhang, X. *et al.* Multiscale understanding and architecture design of high energy/power lithium-ion battery electrodes. *Adv. Energy Mater.* **11**, 2000808 (2021).

39. Chao, C.-H. *et al.* Roll-to-roll atomic layer deposition of titania coating on polymeric separators for lithium ion batteries. *J. Power Sources* **482**, 228896 (2021).

40. Barbosa, J. C. *et al.* Enhanced ionic conductivity in poly(vinylidene fluoride) electrospun separator membranes blended with different ionic liquids for lithium ion batteries. *J. Colloid Interface Sci.* **582**, 376–386 (2021).

41. Li, F.-S., Wu, Y.-S., Chou, J., Winter, M. & Wu, N.-L. A mechanically robust and highly ion-conductive polymer-blend coating for high-power and long-life lithium-ion battery anodes. *Adv. Mater.* **27**, 130–137 (2015).

42. Zhao, F., Shi, Y., Pan, L. & Yu, G. Multifunctional Nanostructured Conductive Polymer Gels: Synthesis, Properties, and Applications. *Acc. Chem. Res.* **50**, 1734–1743 (2017).

43. Yanik, M. O., Yigit, E. A., Akansu, Y. E. & Sahmetlioglu, E. Magnetic conductive polymer-graphene nanocomposites based supercapacitors for energy storage. *Energy* **138**, 883–889 (2017).

44. Wang, Q., Jiang, L., Yu, Y. & Sun, J. Progress of enhancing the safety of lithium ion battery from the electrolyte aspect. *Nano Energy* **55**, 93–114 (2019).

45. Zhang, S. S. A review on electrolyte additives for lithium-ion batteries. *J. Power Sources* **162**, 1379–1394 (2006).

46. Haregewoin, A. M., Wotango, A. S. & Hwang, B.-J. Electrolyte additives for lithium ion battery electrodes: progress and perspectives. *Energy Environ. Sci.* **9**, 1955–1988 (2016).

47. Berckmans, G. *et al.* Cost Projection of State of the Art Lithium-Ion Batteries for Electric Vehicles Up to 2030. *Energies* **10**, 1314 (2017).

48. Teki, R. *et al.* Nanostructured silicon anodes for lithium ion rechargeable batteries. *Small* **5**, 2236–2242 (2009).

49. Li, X. *et al.* Mesoporous silicon sponge as an anti-pulverization structure for high-performance lithium-ion battery anodes. *Nat. Commun.* **5**, 4105 (2014).

50. He, Y., Yu, X., Wang, Y., Li, H. & Huang, X. Alumina-coated patterned amorphous silicon as the anode for a lithium-ion battery with high Coulombic efficiency. *Adv. Mater.* **23**, 4938–4941 (2011).

51. Yin, Y.-X., Xin, S., Guo, Y.-G. & Wan, L.-J. Lithium-sulfur batteries: electrochemistry, materials, and prospects. *Angew. Chem. Int. Ed Engl.* **52**, 13186–13200 (2013).

52. Manthiram, A., Chung, S.-H. & Zu, C. Lithium-sulfur batteries: progress and prospects. *Adv. Mater.* **27**, 1980–2006 (2015).

53. Ma, L., Hendrickson, K. E., Wei, S. & Archer, L. A. Nanomaterials: Science and applications in the lithium–sulfur battery. *Nano Today* **10**, 315–338 (2015).

54. Rosenman, A. *et al.* Review on Li-sulfur battery systems: An integral perspective. *Adv. Energy Mater.* **5**, 1500212 (2015).

55. Pope, M. A. & Aksay, I. A. Structural design of cathodes for Li-S batteries. *Adv. Energy Mater.* **5**, 1500124 (2015).

56. Ji, X., Lee, K. T. & Nazar, L. F. A highly ordered nanostructured carbon–sulphur cathode for lithium–sulphur batteries. *Nat. Mater.* **8**, 500–506 (2009).

57. Xin, S. *et al.* Smaller Sulfur Molecules Promise Better Lithium–Sulfur Batteries. *J. Am. Chem. Soc.* **134**, 18510–18513 (2012).

58. Jayaprakash, N., Shen, J., Moganty, S. S., Corona, A. & Archer, L. A. Porous Hollow Carbon@Sulfur Composites for High-Power Lithium-Sulfur Batteries. *Angewandte Chemie* vol. 123 6026–6030 (2011).

59. He, G. *et al.* Tailoring Porosity in Carbon Nanospheres for Lithium–Sulfur Battery Cathodes. *ACS Nano* **7**, 10920–10930 (2013).

60. Strubel, P. *et al.* ZnO hard templating for synthesis of hierarchical porous carbons with tailored porosity and high performance in lithium-sulfur battery. *Adv. Funct. Mater.* **25**, 287–297 (2015).

61. Reneker, D. H. & Chun, I. Nanometre diameter fibres of polymer, produced by electrospinning. *Nanotechnology* **7**, 216 (1999).

62. Huang, Z.-M., Zhang, Y.-Z., Kotaki, M. & Ramakrishna, S. A review on polymer nanofibers by electrospinning and their applications in nanocomposites. *Compos. Sci. Technol.* **63**, 2223–2253 (2003).

63. Reneker, D. H., Yarin, A. L., Fong, H. & Koombhongse, S. Bending instability of electrically charged liquid jets of polymer solutions in electrospinning. *J. Appl. Phys.* **87**, 4531–4547 (2000).

64. Li, D. & Xia, Y. Electrospinning of nanofibers: reinventing the wheel? *Adv. Mater.* (2004).

65. Engine and Industrial Air, Oil and Liquid Filtration | Donaldson Company, Inc. https://www.donaldson.com/en-us/.

66. Frenot, A. & Chronakis, I. S. Polymer nanofibers assembled by electrospinning. *Curr. Opin. Colloid Interface Sci.* **8**, 64–75 (2003).

67. Mahalingam, S., Raimi-Abraham, B. T., Craig, D. Q. M. & Edirisinghe, M. Solubility–spinnability map and model for the preparation of fibres of polyethylene (terephthalate) using gyration and pressure. *Chem. Eng. J.* **280**, 344–353 (2015).

68. Kim, C. *et al.* Raman spectroscopic evaluation of polyacrylonitrile-based carbon nanofibers prepared by electrospinning. *J. Raman Spectrosc.* **35**, 928–933 (2004).

69. Kim, C. *et al.* Synthesis and characterization of porous carbon nanofibers with hollow cores through the thermal treatment of electrospun copolymeric nanofiber webs. *Small* **3**, 91–95 (2007).

70. McCann, J. T. *et al.* Carbon nanotubes by electrospinning with a polyelectrolyte and vapor deposition polymerization. *Nano Lett.* **7**, 2470–2474 (2007).

71. Zhu, C., Tong, N., Song, L. & Zhang, G. Investigation of Raman spectra of polyethylene terephthalate. *International Symposium on Photonics and Optoelectronics 2015* (2015) doi:10.1117/12.2205157.

72. Tong N. *et al.* Characteristics of Raman spectra of polyethylene terephthalate. *Guang Pu Xue Yu Guang Pu Fen Xi* **36**, 114–118 (2016).

73. Sheng, C. Char structure characterised by Raman spectroscopy and its correlations with combustion reactivity. *Fuel* **86**, 2316–2324 (2007).

74. Schwan, J., Ulrich, S., Batori, V., Ehrhardt, H. & Silva, S. R. P. Raman spectroscopy on amorphous carbon films. *J. Appl. Phys.* **80**, 440–447 (1996).

75. Ferrari, A. C., Robertson, J., Ferrari, A. C. & Robertson, J. Raman spectroscopy of amorphous, nanostructured, diamond–like carbon, and nanodiamond. *Philosophical Transactions of the Royal Society of London. Series A: Mathematical, Physical and Engineering Sciences* **362**, 2477–2512 (2004).

76. Thakur, S. & Karak, N. Green reduction of graphene oxide by aqueous phytoextracts. *Carbon N. Y.* **50**, 5331–5339 (2012).

77. Hidayah, N. M. S. *et al.* Comparison on graphite, graphene oxide and reduced graphene oxide: Synthesis and characterization. *AIP Conf. Proc.* **1892**, 150002 (2017).

78. Dresselhaus, M. S., Jorio, A., Hofmann, M., Dresselhaus, G. & Saito, R. Perspectives on carbon nanotubes and graphene Raman spectroscopy. *Nano Lett.* **10**, 751–758 (2010).

79. Rajan, A. S., Sampath, S. & Shukla, A. K. An in situ carbon-grafted alkaline iron electrode for iron-based accumulators. *Energy & Environmental Science* vol. 7 1110 (2014).

80. Some, S. *et al.* High-quality reduced graphene oxide by a dual-function chemical reduction and healing process. *Sci. Rep.* **3**, 1929 (2013).

81. Ci, L. *et al.* Crystallization behavior of the amorphous carbon nanotubes prepared by the CVD method. *J. Cryst. Growth* **233**, 823–828 (2001).

82. Jurkiewicz, K., Pawlyta, M. & Burian, A. Structure of Carbon Materials Explored by Local Transmission Electron Microscopy and Global Powder Diffraction Probes. *C—Journal of Carbon Research* **4**, 68 (2018).

83. Song, S. *et al.* Facile self-templating large scale preparation of biomass-derived 3D hierarchical porous carbon for advanced supercapacitors. *J. Mater. Chem. A Mater. Energy Sustain.* **3**, 18154–18162 (2015).

84. Chen, Z. *et al.* High-performance sodium-ion pseudocapacitors based on hierarchically porous nanowire composites. *ACS Nano* **6**, 4319–4327 (2012).

85. Gong, Y., Li, D., Fu, Q. & Pan, C. Influence of graphene microstructures on electrochemical performance for supercapacitors. *Progress in Natural Science: Materials International* **25**, 379–385 (2015).

86. Wang, W. *et al.* Hydrous ruthenium oxide nanoparticles anchored to graphene and carbon nanotube hybrid foam for supercapacitors. *Sci. Rep.* **4**, 4452 (2014).

87. Fan, Z. *et al.* A three-dimensional carbon nanotube/graphene sandwich and its application as electrode in supercapacitors. *Adv. Mater.* **22**, 3723–3728 (2010).

88. Zhang, L. L. & Zhao, X. S. Carbon-based materials as supercapacitor electrodes. *Chem. Soc. Rev.* **38**, 2520–2531 (2009).

89. Conway, B. E., Birss, V. & Wojtowicz, J. The role and utilization of pseudocapacitance for energy storage by supercapacitors. *J. Power Sources* **66**, 1–14 (1997).

90. Ahmed, S., Ahmed, A. & Rafat, M. Supercapacitor performance of activated carbon derived from rotten carrot in aqueous, organic and ionic liquid based electrolytes. *Journal of Saudi Chemical Society* **22**, 993–1002 (2018).

91. Seredych, M., Hulicova-Jurcakova, D., Lu, G. Q. & Bandosz, T. J. Surface functional groups of carbons and the effects of their chemical character, density and accessibility to ions on electrochemical performance. *Carbon N. Y.* **46**, 1475–1488 (2008).

92. Yang, I., Kim, S.-G., Kwon, S. H., Kim, M.-S. & Jung, J. C. Relationships between pore size and charge transfer resistance of carbon aerogels for organic electric double-layer capacitor electrodes. *Electrochim. Acta* **223**, 21–30 (2017).

93. Raja, M., Angulakshmi, N. & Manuel Stephan, A. Sisal-derived activated carbons for cost-effective lithium–sulfur batteries. *RSC Adv.* **6**, 13772–13779 (2016).

94. Lota, K., Acznik, I., Sierczynska, A. & Lota, G. The capacitance properties of activated carbon obtained from chitosan as the electrode material for electrochemical capacitors. *Mater. Lett.* **173**, 72–75 (2016).

95. Sun, P. *et al.* Poly(ethylene terephthalate): Rubbish could be low cost anode material of lithium ion battery. *Solid State Ionics* **317**, 164–169 (2018).

96. Półrolniczak, P. *et al.* Composite sulfur cathode for Li-S batteries comprising hierarchical carbon obtained from waste PET bottles. *Synth. Met.* **261**, 116305 (2020).

97. Ghosh, S. *et al.* Rapid Upcycling of Waste Polyethylene Terephthalate to Energy Storing Disodium Terephthalate Flowers with DFT Calculations. *ACS Sustainable Chem. Eng.* **8**, 6252–6262 (2020).

98. Ko, S., Kwon, Y. J., Lee, J. U. & Jeon, Y.-P. Preparation of synthetic graphite from waste PET plastic. *J. Ind. Eng. Chem.* **83**, 449–458 (2020).

99. Kim, K. S. *et al.* The effect of waste PET addition on PFO-based anode materials for improving the electric capacity in lithium-ion battery. *Carbon Letters* 1–9 (2020).

100. Aradi, B., Hourahine, B. & Frauenheim, T. DFTB+, a sparse matrix-based implementation of the DFTB method. *J. Phys. Chem. A* **111**, 5678–5684 (2007).

101. Rauls, E., Elsner, J., Gutierrez, R. & Frauenheim, T. Stoichiometric and non-stoichiometric $(10\bar{1}0)$ and $(11\bar{2}0)$ surfaces in 2H–SiC: a theoretical study. *Solid State Commun.* **111**, 459–464 (1999).

102. Köhler, C., Hajnal, Z., Deák, P., Frauenheim, T. & Suhai, S. Theoretical investigation of carbon defects and diffusion in α-quartz. *Phys. Rev. B Condens. Matter* **64**, (2001).

103. Sieck, A., Frauenheim, T. & Jackson, K. A. Shape transition of medium-sized neutral silicon clusters. *Phys. Status Solidi B Basic Res.* **240**, 537–548 (2003).

104. Vuong, V. Q. *et al.* Parametrization and Benchmark of Long-Range Corrected DFTB2 for Organic Molecules. *J. Chem. Theory Comput.* **14**, 115–125 (2018).

105. Tehrani, F. S. Transformation from amorphous to nano-crystalline SiC thin films prepared by HWCVD technique without hydrogen dilution. *Bull. Mater. Sci.* **38**, 1333–1338 (2015).

106. Borowicz, P. *et al.* Deep-ultraviolet Raman investigation of silicon oxide: thin film on silicon substrate versus bulk material. *Adv. Nat. Sci: Nanosci. Nanotechnol.* **3**, 045003 (2012).

107. Gogotsi, Y., Zhou, G., Ku, S.-S. & Cetinkunt, S. Raman microspectroscopy analysis of pressure-induced metallization in scratching of silicon. *Semiconductor Science and Technology* vol. 16 345–352 (2001).

108. Temple, P. A. & Hathaway, C. E. Multiphonon Raman Spectrum of Silicon. *Phys. Rev. B Condens. Matter* **7**, 3685–3697 (1973).

109. Meier, C. *et al.* Raman properties of silicon nanoparticles. *Physica E* **32**, 155–158 (2006).

110. Huang, Y. *et al.* UV-Raman scattering of thin film Si with ultrathin silicon oxide tunnel contact for high efficiency crystal silicon solar cells. *Sol. Energy Mater. Sol. Cells* **192**, 154–160 (2019).

111. Geissberger, A. E. & Galeener, F. L. Raman studies of vitreous SiO2versus fictive temperature. *Phys. Rev. B Condens. Matter* **28**, 3266–3271 (1983).

112. Ossonon, B. D. & Bélanger, D. Synthesis and characterization of sulfophenyl-functionalized reduced graphene oxide sheets. *RSC Adv.* **7**, 27224–27234 (2017).

113. Font, J., Muntasell, J. & Cesari, E. Poly(butylene terephthalate) poly(ethylene terephthalate) mixtures formed by ball milling. *Mater. Res. Bull.* **34**, 157–165 (1999).

114. Lamba, D. Wide-Angle X-ray Diffraction Pattern. *Encyclopedia of Membranes* 1–2 (2014) doi:10.1007/978-3-642-40872-4_1099-1.

115. Štokr, J., Schneider, B., Doskočilová, D., Lövy, J. & Sedláček, P. Conformational structure of poly (ethylene terephthalate). Infra-red, Raman and nmr spectra. *Polymer* **23**, 714–721 (1982).

116. Chen, Y., Zhang, X., Tian, Y. & Zhao, X. Synthesis and Characterization of Silicon Nanoparticles Inserted into Graphene Sheets as High Performance Anode Material for Lithium Ion Batteries. *J. Nanomater.* **2014**, (2014).

117. Oh, H. S., Jeong, H. M., Park, J. H., Ock, I.-W. & Kang, J. K. Hierarchical Si hydrogel architecture with conductive polyaniline channels on sulfonated-graphene for high-performance Li ion battery anodes having a robust cycle life. *J. Mater. Chem. A Mater. Energy Sustain.* **3**, 10238–10242 (2015).

118. Magasinski, A. *et al.* High-performance lithium-ion anodes using a hierarchical bottom-up approach. *Nat. Mater.* **9**, 353–358 (2010).

119. Li, W. *et al.* Core-shell Si/C nanospheres embedded in bubble sheet-like carbon film with enhanced performance as lithium ion battery anodes. *Small* **11**, 1345–1351 (2015).

120. Zhou, X., Yin, Y.-X., Wan, L.-J. & Guo, Y.-G. Facile synthesis of silicon nanoparticles inserted into graphene sheets as improved anode materials for lithium-ion batteries. *Chemical Communications* vol. 48 2198 (2012).

121. Jerliu, B. *et al.* Lithium insertion into silicon electrodes studied by cyclic voltammetry and operando neutron reflectometry. *Phys. Chem. Chem. Phys.* **20**, 23480–23491 (2018).

122. Ge, M. *et al.* Scalable preparation of porous silicon nanoparticles and their application for lithium-ion battery anodes. *Nano Res.* **6**, 174–181 (2013).

123. Green, M., Fielder, E. & Scrosati, B. Structured silicon anodes for lithium battery applications. *and Solid-State …* (2003).

124. Kasavajjula, U., Wang, C. & John Appleby, A. Nano- and bulk-silicon-based insertion anodes for lithium-ion secondary cells. *Journal of Power Sources* vol. 163 1003–1039 (2007).

125. Wang, B. *et al.* Adaptable Silicon–Carbon Nanocables Sandwiched between Reduced Graphene Oxide Sheets as Lithium Ion Battery Anodes. *ACS Nano* **7**, 1437–1445 (2013).

126. Li, J. & Dahn, J. R. An in situ X-ray diffraction study of the reaction of Li with crystalline Si. *J. Electrochem. Soc.* **154**, A156–A161 (2007).

127. Chen, Y. *et al.* Hollow Carbon-Nanotube/Carbon-Nanofiber Hybrid Anodes for Li-Ion Batteries. *Journal of the American Chemical Society* vol. 135 16280–16283 (2013).

128. Mirjalili, A., Dong, B., Pena, P., Ozkan, C. S. & Ozkan, M. Upcycling of Polyethylene Terephthalate Plastic Waste to Microporous Carbon Structure for Energy Storage. *Energy Storage* (2020) doi:10.1002/est2.201.

129. Sebastian, S. S. *et al.* Adaptive fast charging methodology for commercial Li-ion batteries based on the internal resistance spectrum. *Energy Storage* **2**, (2020).

130. Zhu, J. G., Sun, Z. C., Wei, X. Z. & Dai, H. F. A new electrochemical impedance spectroscopy model of a high-power lithium-ion battery. *RSC Adv.* **4**, 29988–29998 (2014).

131. Wang, C., Appleby, A. J. & Little, F. E. Electrochemical impedance study of initial lithium ion intercalation into graphite powders. *Electrochim. Acta* **46**, 1793–1813 (2001).

132. Zhu, Y. & Wang, C. Galvanostatic Intermittent Titration Technique for Phase-Transformation Electrodes. *J. Phys. Chem. C* **114**, 2830–2841 (2010).

133. Jung, I. *et al.* Reduction Kinetics of Graphene Oxide Determined by Electrical Transport Measurements and Temperature Programmed Desorption. *J. Phys. Chem. C* **113**, 18480–18486 (2009).

134. Best, S. *et al.* Evidence for Glass Behavior in Amorphous Carbon. *C — Journal of Carbon Research* **6**, 50 (2020).

135. Bell, J. *et al.* Plateau targeted conditioning: An additive-free approach towards robust SEI formation in Li-S batteries for enhanced capacity and cycle life. *Nano Energy* **49**, 498–507 (2018).

136. Zhang, J., Yang, C.-P., Yin, Y.-X., Wan, L.-J. & Guo, Y.-G. Sulfur encapsulated in graphitic carbon nanocages for high-rate and long-cycle lithium-sulfur batteries. *Adv. Mater.* **28**, 9539–9544 (2016).

137. Cheng, Y. *et al.* Flexible and cross-linked N-doped carbon nanofiber network for high performance freestanding supercapacitor electrode. *Nano Energy* **15**, 66–74 (2015).

138. Zhan, C., Zhang, Y., Cummings, P. T. & Jiang, D.-E. Enhancing graphene capacitance by nitrogen: effects of doping configuration and concentration. *Phys. Chem. Chem. Phys.* **18**, 4668–4674 (2016).

139. Radovic, L. R., Karra, M., Skokova, K. & Thrower, P. A. The role of substitutional boron in carbon oxidation. *Carbon N. Y.* **36**, 1841–1854 (1998).

140. Lee, Y.-J., Uchiyama, Y. & Radovic, L. R. Effects of boron doping in low- and high-surface-area carbon powders. *Carbon N. Y.* **42**, 2233–2244 (2004).

141. Wang, D.-W., Li, F., Chen, Z.-G., Lu, G. Q. & Cheng, H.-M. Synthesis and Electrochemical Property of Boron-Doped Mesoporous Carbon in Supercapacitor. *Chem. Mater.* **20**, 7195–7200 (2008).

142. Hulicova-Jurcakova, D. *et al.* Highly stable performance of supercapacitors from phosphorus-enriched carbons. *J. Am. Chem. Soc.* **131**, 5026–5027 (2009).

143. Wen, Y., Wang, B., Huang, C., Wang, L. & Hulicova-Jurcakova, D. Synthesis of phosphorus-doped graphene and its wide potential window in aqueous supercapacitors. *Chem.--Eur. J.* **21**, 80–85 (2015).

144. Elessawy, N. A., El Nady, J., Wazeer, W. & Kashyout, A. B. Development of High-Performance Supercapacitor based on a Novel Controllable Green Synthesis for 3D Nitrogen Doped Graphene. *Sci. Rep.* **9**, 1129 (2019).

145. Zhang, F. *et al.* Hierarchically porous carbon foams for electric double layer capacitors. *Nano Res.* **9**, 2875–2888 (2016).

146. Cai, M., Thorpe, D., Adamson, D. H. & Schniepp, H. C. Methods of graphite exfoliation. *J. Mater. Chem.* **22**, 24992–25002 (2012).

147. Han, J. T. *et al.* Extremely efficient liquid exfoliation and dispersion of layered materials by unusual acoustic cavitation. *Sci. Rep.* **4**, 5133 (2014).

148. Hernandez, Y. *et al.* High-yield production of graphene by liquid-phase exfoliation of graphite. *Nat. Nanotechnol.* **3**, 563–568 (2008).

149. Wang, W. *et al.* A Novel Exfoliation Strategy to Significantly Boost the Energy Storage Capability of Commercial Carbon Cloth. *Adv. Mater.* **27**, 3572–3578 (2015).

150. Hao, L., Li, X. & Zhi, L. Carbonaceous electrode materials for supercapacitors. *Adv. Mater.* **25**, 3899–3904 (2013).

151. Fic, K., Frackowiak, E. & Béguin, F. Unusual energy enhancement in carbon-based electrochemical capacitors. *J. Mater. Chem.* **22**, 24213–24223 (2012).

152. Chmiola, J. *et al.* Anomalous increase in carbon capacitance at pore sizes less than 1 nanometer. *Science* **313**, 1760–1763 (2006).

153. Lin, R. *et al.* Capacitive energy storage from −50 to 100 °C using an ionic liquid electrolyte. *J. Phys. Chem. Lett.* **2**, 2396–2401 (2011).